Engineering versatile Au-based catalysts for solar-to-fuel conversion

Chunhua Wang,[1,3] Hongwen Zhang,[2] Feili Lai,[1] Zhirun Xie,[3] Yun Hau Ng,[3] Yuhe Liao,[4,*] Xuejiao Wu,[5] Bo Weng[2,*]

[1] *Department of Chemistry, KU Leuven, Celestijnenlaan 200F, 3001 Leuven, Belgium*

[2] *cMACS, Department of Microbial and Molecular Systems, KU Leuven, Celestijnenlaan 200F, 3001 Leuven, Belgium*

[3] *School of Energy and Environment, City University of Hong Kong, 83 Tat Chee Avenue, Kowloon, Hong Kong SAR, China*

[4] *Guangzhou Institute of Energy Conversion, Chinese Academy of Sciences, No. 2, Nengyuan, Road, Tianhe District, Guangzhou 510640, China*

[5] *Centre for Sustainable Catalysis and Engineering, Faculty of Bioscience Engineering, KU Leuven, 3001 Leuven, Belgium*

[*]Corresponding authors.

E-mail: liaoyh@ms.giec.ac.cn or yuhe.liao20@ms.giec.ac.cn; bo.weng@kuleuven.be

Abstract

Gold (Au) nanostructures (NSs) have been widely employed as co-catalysts to improve the photoactivity of semiconductor materials, while a systematic summary of the engineering approaches of Au NSs to maximize the solar-to-fuel conversion efficiency is still lacking. In this review, the recently developed strategies for elevating the overall photocatalytic performance of Au-based photocatalysts and the deep physical chemistry mechanisms are highlighted. Firstly, the synthetic approaches of Au NSs are summarized, followed by an elaboration on their multiple functions in improving photoactivity. Afterward, the modification strategies of Au NSs used to enhance the photocatalytic efficiency of Au-semiconductor composites, including controlling the Au NS morphology, size, crystal phase, defect engineering, alloying with different metals, modulating interfacial interaction, and introducing an external field, are summarized and discussed independently. Finally, we share our opinion on the challenges and outline potentially promising opportunities and directions for efficient Au-based photocatalysis research moving forward. We sincerely look forward to this review can deliver insightful views to design efficient Au-based photocatalysts and spur certain innovations to other metal-based catalysts.

Keywords: Au nanostructures; Modification strategies; Semiconductor; Photocatalysis; Solar-to-fuel conversion

1. Introduction

Abating the excessive utilization of fossil fuels is a major challenge in the development of a sustainable society [1, 2]. In this regard, it is urgent to explore clean and green energy resources, such as solar energy, to replace fossil fuels [3-6]. Among the various options to utilize the abundant solar energy, semiconductor-based photocatalysis, which can directly harvest energy from sunlight and convert it into chemicals and fuels, attracted considerable attention since the pioneering work of Honda and Fujishima in 1972 [7]. Especially, photocatalytic fuel generation, such as water splitting, has been regarded as one of the most promising strategies for addressing the growing demand for renewable and clean energy resources to simultaneously alleviate energy and environmental issues [8-10].

Generally, the semiconductor-based photocatalytic process can be divided into three consecutive steps [5, 11]: (i) the incident photons with sufficient energies can be absorbed by the semiconductor to generate electron-hole pairs; (ii) the photogenerated charge carriers separate and migrate from the bulk to the surface of the semiconductor; and (iii) the reduction and oxidation reactions occur on the semiconductor's surface triggered by electrons and holes, respectively. To date, diverse semiconductor-based photocatalysts have been reported including TiO_2, C_3N_4, CdS, etc. [12-14], for solar energy conversion. Unfortunately, single semiconductor photocatalysts generally suffer from unsatisfactory solar-to-fuel conversion efficiency due to the unwanted recombination of photogenerated electron-hole pairs and the lack of surface reaction sites [5, 15]. To address these issues, enormous efforts have been devoted to developing efficient photocatalysts by loading cocatalysts, constructing heterojunctions, and controlling morphology and crystallinity [3, 5]. Among these strategies, the introduction of cocatalysts such as noble metals (Au, Pt, Pd) [16-18], metal sulfides (MoS_2, NiS, CoS) [19-21], and metal oxides (NiO_2, WO_3, Cu_2O) [22-24], has been widely adopted.

Coupling semiconductors with noble metal cocatalysts has been claimed to have multiple benefits, including improving light absorption, reducing reaction barriers, increasing the number of reactive sites, inhibiting electron-hole pair recombination, and regulating product selectivity [3, 8]. Particularly, Au as a stable and durable noble metal and interesting catalytic and optical properties has been extensively studied. The blooming interest in the arena of Au-based photocatalysis is confirmed by an advanced search using "Au photocatalysis" as the topic keyword in the Web of Science database.

As shown in **Fig. 1**, the number of publications on Au photocatalysis has drastically skyrocketed over the past four decades, especially within these 10 years. This endows Au NSs realizable and applicable for solar-to-fuel conversion, thus presenting a whole picture of the current status and the future research direction in this field is meaningful.

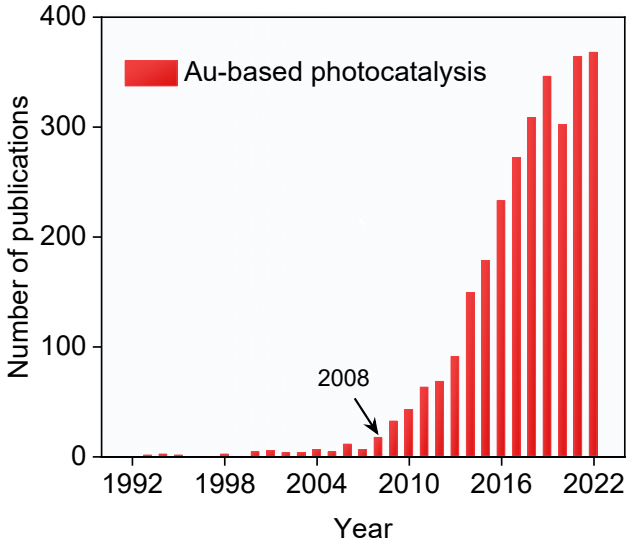

Fig. 1. The number of publications on Au-based photocatalysis from 1990 to 2022 obtained using the Web of Science database.

Until now, the functions and applications of metallic Au in photocatalysis have been summarized in some reviews [8, 25, 26]. For instance, Liu et al. reviewed the optical properties of plasmonic metals (Ag, Au, Cu) [25], and their roles in water splitting, photosynthesis, and molecular activation applications. Linic et al. clarified plasmon-enhanced water splitting over metal (Ag, Au)/semiconductor photocatalysts and proposed the needed advancements in plasmon-mediated photocatalysis [26]. However, in these reviews, the introduction of Au nanostructures (NSs) only occupies a small part, and engineering Au NSs for boosting the solar-to-fuel conversion efficiency of semiconductors is not elaborated. Recently, Zhu et al. reviewed Au-based composites for various photocatalytic applications including energy, environment, and organic chemistry [8]. Notably, they mainly focused on the different photocatalytic applications of Au clusters, while the corresponding Au/semiconductor photocatalysts are rarely discussed. There is no review summarizing the strategies and physical chemistry mechanisms for optimizing Au NSs components in Au-based photocatalysts to enhance the overall solar-to-fuel conversion efficiency. Considering the importance of this research field, the recent progress in the field of Au and engineered Au NSs as

enhancers of photocatalytic solar-to-fuel is critically reviewed.

In this review, we evaluated the recent reports in engineering Au-based composites for photocatalytic solar-to-fuel conversion, including CO_2 reduction and H_2 generation. We began with a brief introduction to the various synthetic approaches used for synthesizing different Au NSs. Subsequently, the five major mechanisms (reservoir for photoelectrons, hot electron injection, plasmonic near-field effect, light scattering, and local heating) behind the enhancement of the photocatalytic efficiency over Au-based photocatalysts are presented and critically evaluated. Then, we comprehensively discussed the reported strategies of Au NSs modification that can further improve the photocatalytic performance in solar-to-fuel conversion, focusing on adjusting the NS morphology, controlling NS size, engineering the crystal phase and defects, metal alloying, modulating interfacial interaction, and the introduction of an external field. In the end, we gave perspective on the challenges and opportunities in fabricating efficient Au-based photocatalysts for artificial solar-to-fuel generation. This review aims to deliver insightful views and stimulate more attention to Au-based catalysts toward efficient solar-driven photocatalytic reactions and offers valuable guidance for constructing highly efficient solar-to-fuel conversion systems of other noble metal-based photocatalysts.

2. Synthesis of Au nanostructures

2.1 Physical methods

Several physical methods have been developed to synthesize Au NSs and control their physical properties by controlling the synthetic conditions [27-33]. External energy sources are used to generate Au NS from bulk metal which is irradiated with photons of various energies spanning from γ-rays down to microwaves but also the use of acoustic waves. With γ-rays irradiation, high purity and uniform Au nanoparticles with controllable size in the range of 5-40 nm can be obtained [27]. With microwave irradiation, one can prepare Au NSs via the heating effect [32]. Radiolysis is another useful technique, by which the Au NSs can be possibly enlarged to the desired size [28]. UV irradiation has been an auxiliary approach to control the size and shape of Au NSs [29]. Using laser irradiation to break down bulk material into smaller NSs through high energy emitting lasers (such as a 532 nm laser), the Au with tunable features, i.e., reshaping, fragmentation and assembly can be obtained [33]. The acoustic wave method has been reported to control the Au generation rate by tuning the ultrasound frequency,

and then the size- and shape-controlled Au NSs can be obtained [30, 31].

2.2 (Electro)chemical methods

2.2.1 Colloidal synthesis. Colloidal synthesis of Au NSs is generally performed through the reduction of an aqueous chloruretic solution with a stabilizing agent. Several reducing agents such as citrate [34], sodium borohydride [35], and sodium ascorbate [36], are commonly used to reduce Au(III) ions to Au(0). The chemical reduction generally involves one or more water-soluble polymers, surfactants, or capping agents that help to provide high stability and prevent the aggregation of Au NSs. Among various methods, the Turkevich procedure is widely adopted due to its simplicity, controllable size, and stable colloidal nanoparticles [37]. Most importantly, the Au NSs synthesized via the Turkevich method generally exhibit a narrow size distribution [38]. Following the Brust-Schiffrin method reported in 1994, utilizing potent thiol-gold interactions to protect the Au NSs was also widely adopted, among which Au NSs with controlled shapes, sizes, and surface properties can be produced via manipulating surface-modifying agents, salt concentration, or reaction conditions [39]. Specifically, through a seed-mediated growth process, uniform quasi-spherical Au with a wide range of sizes from 10 to 200 nm [40], Au nanorods with controllable aspect ratios, and Au NSs with icosahedron, icosidodecahedron and dodecahedron shapes via tuning the facets of Au seeds, have been synthesized.

Recently, unconventional Au NSs (non-fcc Au), including hcp 2H, 4H, bct, and bco phases, have also been reported [41, 42]. Zhang's group has developed many different strategies for the synthesis of hcp-Au NSs that are stable under ambient conditions. For example, 2H phase Au sheets with a diameter of 200-500 nm and thickness of ca. 2.4 nm were achieved with the support of graphene oxide [43]. 4H Au nanoribbons were synthesized with a template-free approach in a [Au(I)-oleylamine] complex with the additive of 1,2-dichloropropane, in which the Au nanoribbons can be mediated in a large size range with the width of 15-61 nm, length of 0.5-6.0 μm, and thickness of 2.0-6.0 nm [44].

2.2.2 Electrochemical methods. The electrochemical synthesis of Au NSs is usually performed using a two-electrode cell, with oxidation of the anode and reduction of the cathode [45]. This method has the advantages of good quality, rapid fabrication, low temperature, without additives, and easy control of the yield [46, 47]. The size of the

Au NSs can be tuned by the management of the surfactant concentration, growth temperature and current density. For instance, by utilizing ionic surfactants (hexadecyltrimethylammonium bromide) as both supporting electrolytes and stabilizers, Au nanorods with different aspect ratios were synthesized [48]. Furthermore, hierarchical flowerlike Au microstructures (nanoplates or nanoprisms) on indium tin oxide substrates were produced without a template and surfactant, where the diameters of Au are governable through mediating the deposition time or the deposition potential (vs. Ag/AgCl) [49].

2.3 Biosynthesis methods

Biological methods are considered a clean, non-toxic, and eco-friendly approach for the synthesis of Au NSs [50, 51]. Plant-based microorganisms and derivatives, such as weishen, fungi, algae, yeast, and viruses, have been employed to reduce Au ions under ambient temperature and pressure conditions, and produce Au NSs with various sizes and shapes. For example, $HAuCl_4$ as a precursor can be reduced by citrus fruit juice to fabricate different sizes and shapes of Au nanoparticles [50]. Another green synthesis method of Au NSs with sizes from 15-80 nm was also reported, in which the edible mushroom was used as a biological agent [52]. Also, using natural chitosan without any stabilizers and reductants, Au nanoparticles can be produced from bulk Au substrates [53]. Moreover, the ability to produce Au nanoparticles using the bacterial strain *Bacillus marisflavi* was also reported [51], in which the Au synthesis takes place extracellularly from the cell-free extract of the bacteria within 96 h, along with the color change from pale yellow to bluish purple. Due to surface plasmon resonance, blue-violet coloration occurs confirming the formation of the Au nanoparticles with an average size of *ca.* 10 nm.

2.4 Other methods

In addition to the aforementioned approaches, some other methods have been explored. For instance, the shape controlled Au NSs were obtained using a template method, among which different morphologies of Au NSs, such as nanoboxes [54] and multipod [55], can be produced using Ag nanocrystals as the sacrificial templates. Furthermore, ultrathin two-dimensional Au NSs have been synthesized using template-confined growth methods [56]. In addition, utilizing a one-pot method, nanodisks [57], nanostars [58], nanobelts [59], and nanowires [60], have been reported. Taking nanostar as an

example, the star-shaped Au nanoplates were directly synthesized through the reduction of $HAuCl_4$ aqueous solution by *L*-ascorbic acid with poly(*N*-vinyl-2-pyrrolidone) at room temperature, without the utilization of Au seeds [58]. The color of the solution first changed from pale yellow to colorless due to the reduction of Au(III) to Au(I), and then further turned red-purple within 5 min. After a 5 h reaction, the Au nanostars were produced. Following this strategy, Au platonic NSs [61], and Au enclosed by the high-index facets have also been achieved [62].

3. Mechanisms for photoactivity enhancements

Integration of Au NSs as co-catalysts has been demonstrated to be an effective method to improve the efficiency of single semiconductor photocatalysts [5, 11, 17, 63-65]. Regarding the roles of Au NSs during the photocatalytic reaction process, so far, five major mechanisms have been proposed: (1) photoelectron reservoir, (2) hot electron injection, (3) plasmonic near-field effect, (4) scattering of incident light, and (5) heating effect. The dominating mechanisms highly depend on the physical features of the Au NSs and semiconductors and their spatial arrangement in the hybrid composites. These mechanisms will be summarized and discussed in detail in the following content with some typical examples.

3.1 Photoelectron reservoir

Au NSs served as photoelectron reservoirs have been widely used to suppress charge recombination in semiconductors and elongate the lifetime of the charge carriers, thus improving the overall photocatalytic solar-to-fuel conversion efficiency [16, 66]. Taking an n-type semiconductor/Au system as an example, the Au NSs generally have a lower Fermi energy (E_F) compared to the semiconductor before contact, as shown in **Fig. 2A**. When Au NSs are in close contact with the semiconductor, electrons in the semiconductor will migrate to the Au due to the difference in E_F positions and lead to the band bending of the semiconductor [18, 63]. The charge redistribution between the Au and semiconductor will reach an equilibrium when the Fermi level of Au is equal to that of the semiconductor, thus forming a Schottky barrier and a built-in electric field at the interface. Under light irradiation, the electron-hole pairs generated from the semiconductor will be influenced by the Schottky barrier. More specifically, the photogenerated electrons in the semiconductor can transfer to the Au NSs driven by the built-in electric field at the interface, and the as-formed Schottky barrier will block the

backflow of electrons from the Au NSs to the semiconductor, leading to the efficient separation of photogenerated charge carriers and reducing the recombination of electron-hole pairs (**Fig. 2B**) [5, 67]. Notably, just as a coin has two sides. The height Schottky barrier should not be too high, or it will hinder the transfer of electrons from the semiconductor to Au NSs.

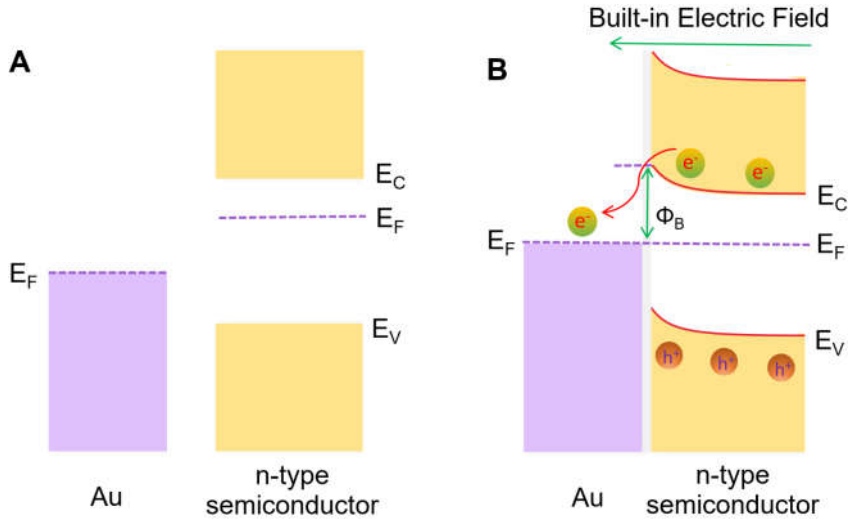

Fig. 2. Schematic band diagram of an n-type semiconductor/Au composite (A) before and (B) after contact. Where, E_F and E_{vac} represent Fermi and vacuum levels, respectively. E_V, E_C, Φ_B, e^-, and h^+ stand for conduction band and valence band energy levels, Schottky barrier energy, and electron and hole, respectively.

3.2 Hot electron injection

Hot electrons in a plasmonic metal refer to the electrons which are not in thermal equilibrium with the atoms, typically with high energy in the range of 1.0-4.0 eV for Au NSs [68, 69], whose distributions can be described by the Fermi function but with an elevated effective temperature. Due to the localized surface plasmon resonance (LSPR) originating from the collective oscillation of surface electrons (**Fig. 3A**) [3, 70], the electromagnetic decay can take place radiatively via re-emitted photons or non-radiatively by transferring the energy to hot electrons (**Fig. 3B**). For the latter one, hot electrons are excited during the non-radiative decay through the intra-band within the conduction band or through the inter-band resulting from transitions between other bands (e.g., d-band) and the conduction band [69, 71]. In terms of Au NSs, because of its relatively low level of *d*-band below the Fermi level (2.4 eV lower than the Fermi energy level), intra-band excitations are preferred to inter-band excitations [69, 72].

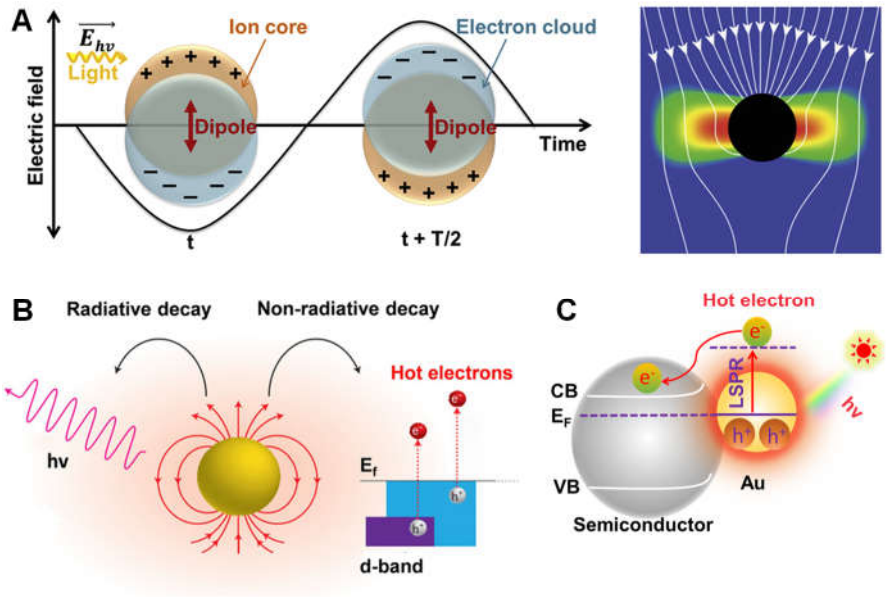

Fig. 3. (A) Schematic illustrating LSPR oscillations induced by an electric field in Au (left) and the energy flux and electric field intensity (right). Reproduced with permission from ref. [3]. Copyright 2018, Elsevier. (B) LSPR decays radiatively via re-emitted photons or non-radiatively via the excitation of hot electrons. Reproduced with permission from ref. [69]. Copyright 2020, Wiley. (C) Scheme of hot-electron injection from Au NSs to the semiconductor.

During the excitation and energy redistribution processes, hot electron transfer may have two different pathways:[73] (1) transfer from the Au to the adsorbed molecules located nearby those Au NSs, to form negative ions (i.e., transient negative ions) which could quickly react on the metal surface or move into the solution; (2) transfer from Au NSs to the neighboring semiconductor. Here we mainly focus on the second one (**Fig. 3C**). The hot electron injection in this pathway is based on the nonradiative decay process of excited plasmons that transfer energy into the semiconductor. This process is usually associated with wide bandgap semiconductors such as TiO_2 and is governed by the semiconductor/Au interface and band alignment. Normally, three requirements are essential for realizing the hot electron injection process:[71]

(1) An intimate interfacial contact between Au NSs and semiconductors provides channels for charge transfer. The hot electron injection is functional in composite photocatalysts, where the Au are in direct contact with the semiconductor intimately, allowing a fast transfer of charge carriers [26]. Another factor is the timescale requirement. The lifetime of hot electrons is in

the timescale of 10-100 ps, much shorter than that of excited electrons in semiconductors (a few to hundreds of fs) [72]. Thus, efficient interfacial contact via structural design is needed, which can enable a fast electron injection to the semiconductor to suppress the decay, and inhibit electron back-injection to Au NSs.

(2) The band alignment between Au and semiconductor. For Au NSs, the LSPR energy is on the scale of 1.0-4.0 eV regarding the Fermi level (0 eV vs. NHE) [26, 74]. Thus, the energetic electron formed via LSPR excitation will be in this energy window. The alignment of electronic states allows for the transfer of energetic electrons from Au NSs to the semiconductor [26].

(3) The energy of hot electrons should be larger than the Schottky barrier. Due to the presence of the Schottky barrier between Au NSs and semiconductors (**Fig. 2B**), it will block electron transfer from Au NSs to semiconductors [69]. Therefore, the excited hot electrons with sufficient energy are the prerequire to inject hot electrons into the semiconductor.

Fast electron injection in the neighboring semiconductor before charge recombination is a key factor for achieving high energy conversion efficiency. In view of the dynamics, the hot electrons relax within 10-100 ps via electron-electron, electron-phonon, and phonon-phonon interactions [69, 75], but the ultrafast hot-electron injection process (a few to hundreds of fs) can be competitive for these events. Furthermore, the hot electron injection is associates with the electron momentum direction [76]. The hot electrons can effectively inject into the semiconductor as their momentum directions mainly point to the semiconductor. Apart from conventional factors (morphology, size and shape), the hybridization of unoccupied states of a particular system can affect the hot-electron injection process [77].

Although hot electrons with high energy can be favorable for photoredox reactions, they may bring about a negative effect on photocatalytic reactions at some time [72]. For instance, for the Au-TiO_2 composite, both the TiO_2 and Au will be excited and generate charge carriers under mixed UV and green light irradiation. Under such circumstances, the LSPR-induced hot electrons will inject from Au NSs to TiO_2 to compensate and even surpass those electrons transferred from TiO_2 to Au, leading to rapid recombination of charge carriers generated in the semiconductor, thus resulting in a drop in photoactivity [78]. Therefore, more attention should be paid to better understand the underlying mechanism and balance the positive and negative roles of

Au NSs when utilizing Au-based composites for photocatalysis.

3.3 Plasmonic near-field effect

Apart from the hot electron injection where the Au NSs are usually in close contact with the semiconductor, hot electrons can be transferred to the semiconductor through a noncontact resonance energy transfer (i.e., electromagnetic resonance) process [79]. When Au NSs absorb incoming photons with the wavelength near their plasmon resonance frequencies, the optical absorption produces a local electric field near the surface of the Au, yielding an enhanced electromagnetic field, which is called near-field enhancement (**Fig. 4A**) [72, 73].

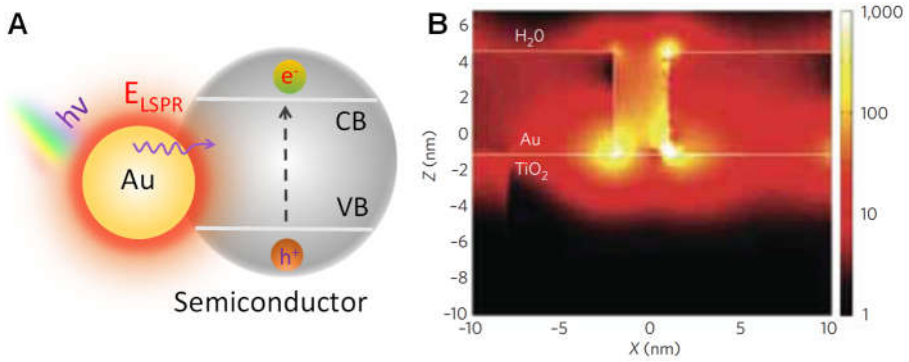

Fig. 4. (A) Scheme of hot electron excitation in the Au/semiconductor system originating from the near-field enhancement. (B) Optical simulations showing LSPR-enhanced electric fields owing to photoexcited Au NSs, permeating into a neighboring TiO_2 material. Reproduced with permission from ref. [80]. Copyright 2011, American Chemical Society.

The important feature of the near-field effect is that the LSPR-induced electron-hole pair formation rate is the highest in the contact parts between the semiconductor and the Au NSs [26]. When near-field energy is higher than the band gap of the adjacent semiconductor, it enables local electron excitation, leading to the formation of charge carriers. Since the formation of electron-hole pairs in a semiconductor is proportional to the intensity of the electric field (specifically, $|E|^2$), the rate of charge production can be significantly increased by several orders of magnitudes compared to that of regular light absorption [73]. The selective formation of charge carriers in the surface region offers some advantages [26]: (1) they are easier to be separated in the presence of surface potential; (2) they have a relatively shorter pathway to reach the active sites and the semiconductor/liquid interface, thus enhancing the probability of participating in

photoredox reactions.

The near-field effect of Au NSs is collaborated by experimental characterizations. As shown in **Fig. 4B**, it can be seen that the rate of electron-hole formation in semiconductors is enhanced in the regions of the proximity of the excited Au NSs [80]. Generally, the energy transfer in this mechanism is influenced by three main factors: (i) the electric field of the incident light, (ii) the overlap between LSPR and optical transitions of the nearby semiconductor, and (iii) the near-field covered volume [72]. The first one greatly determines the energy of the near field, while the latter two factors are significantly affected by the size and shape of Au NSs and the interfacial contact with the semiconductor. Although the near-field effect of Au NSs has been shown to enhance photocatalytic performance, little effort is spent on the direct experimental evidence as well as their corresponding in-depth analyses. Therefore, more experimental technologies need to be introduced to examine the beneficial effect of Au NSs for promoting solar-to-fuel conversion efficiency.

3.4 Light Scattering

Similar to the reports in solar cells or photoelectrochemical cell devices, the light scattering effect of Au NSs is beneficial for improving light absorption, where Au NSs act as nanomirrors that scatter photons that are not absorbed by the semiconductor on the first pass through the composite [26]. The scattered light then penetrates the semiconductor and increases the photon flux (optical path length) in the semiconductor, resulting in enhanced light harvesting (**Fig. 5A**) [81].

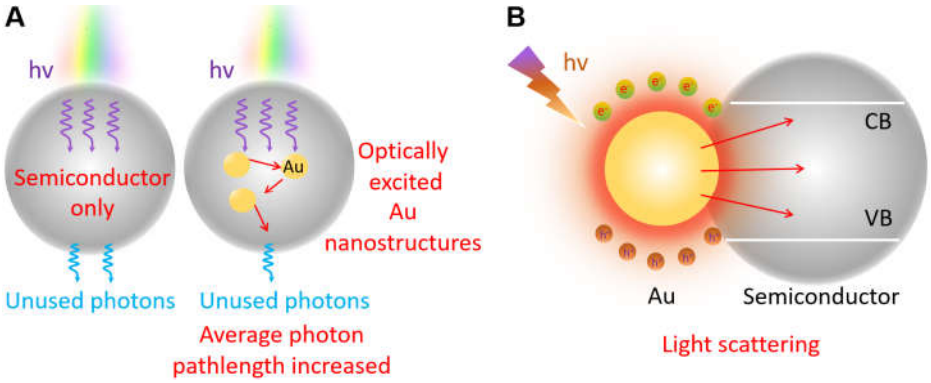

Fig. 5. (A) Schematic illustrating the scattering mechanism. The presence of Au NSs enhances the average path length of photons in the Au-based composite. (B) Light scattering in Au/semiconductor systems.

Photoactivity enhancement originating from the light scattering mechanism is referred to as the increased possibility for the resonant photons to be adsorbed by the semiconductor via vouchsafing more photon-absorption channels to the semiconductor (**Fig. 5B**) [71, 82]. For instance, Sudhagar et al. reported that the decoration of Au nanoparticles on the TiO_2 surface enhanced the light scattering between Au and TiO_2 to promote the light absorbance at the near-UV band [83], thus increasing the generation of electron-hole pairs, and then improving the final photocatalytic performance. Note that the transfer of resonant energy via light scattering occurs for metallic nanostructures with large sizes (> 50 nm) [71]. Since light scattering is a faster process than the absorption process which requires interaction with lattice phonons, its domination will cause a reduction of the light absorption efficiency. It has been reported that light scattering becomes more dominant than absorption when the size of Au is larger than 50 nm [82]. To achieve this mechanism, the wavelength of the resonant-absorption peak must be shorter than the absorption edge of semiconductors, and the size of Au NSs needs to be controlled properly. Apart from the size, the light scattering is strongly associated with the loading amount of Au NSs in the Au-based photocatalysts. Loading a low amount of Au in the composite results in limited multiple scattering and shows negligible optical absorption enhancement, while a high addition content of Au NSs may absorb most of the photons but not for light scattering [84].

3.5 Heating effect

In conjunction with the cascading processes of electron energy spreading, the energy relaxation of photoexcited electrons will increase the temperature of Au NSs, thus heating the local surrounding environment and the semiconductor support and transferring energy to adsorbates [73, 84, 85]. The heating effect of Au NS originates from the non-radiative decay of surface plasmons (**Fig. 3B**). Specifically, under light irradiation, the Au NSs produce abundant charge carriers via LSPR. The relaxation of charge carriers gives rise to a heating effect via electron-electron, electron-phonon, and phonon-phonon interactions [71]. This causes an increase in the temperature in the Au NSs and the surroundings.

Note that the heating effect works more efficiently in small Au NSs (typically below 30 nm). Although such a heating effect does not produce active charge carriers, it is beneficial for photocatalysis since many photochemical reactions go faster at a high temperature [84, 86]. The utilization of Au NSs plasmonic heating effect to perform

chemical reactions is similar to externally heating the system and does not offer a single pathway to control product selectivity [87]. However, it should be noted that the function of plasmonic heating can be dual, that is, a high temperature is unfavorable for the adsorption of absorbates onto Au NSs, while an appropriate temperature can contribute to the activation and transformation of absorbates [71].

4. Engineering Au-based cocatalyst materials in photocatalysis

To improve the reaction efficiency of Au-semiconductor photocatalysts, significant efforts have been concentrated on facilitating the charge transfer process from semiconductor to Au NSs and promoting the injection of plasmonic energy from the Au NSs to semiconductor support via regulating the architecture of the nanohybrids. In this section, various strategies for enhancing the solar-to-fuel conversion efficiency of Au-based composites, including tuning morphology, controlling size, engineering phase and defect, alloying with different metals, modulating interfacial interaction, and introducing external field (**Fig. 6**), will be presented and discussed with some selected examples.

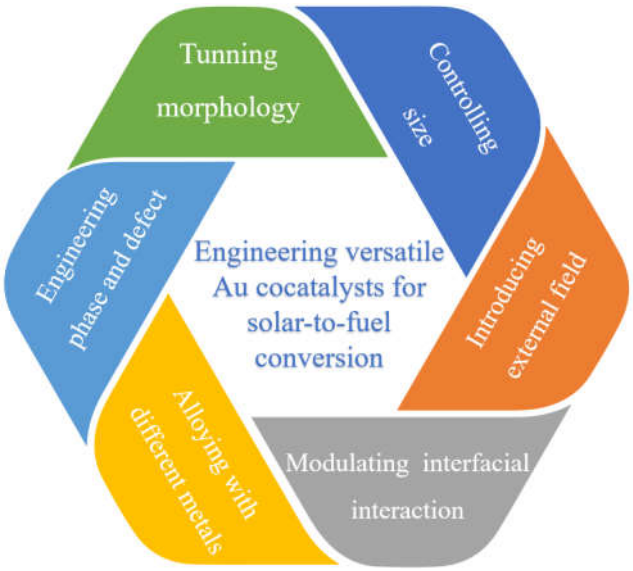

Fig. 6. Diagrams of different strategies for engineering versatile Au cocatalysts for solar-to-fuel conversion.

4.1 Tuning morphology

The morphology of Au NSs has a direct influence on their physical and chemical properties, especially their optical properties, which offers a promising strategy to manipulate the light-harvesting of Au-semiconductor composites and then ameliorate

their photocatalytic performance toward solar-to-fuel conversion [25]. Specifically, the plasmonic resonance of the electron cloud in Au nanospheres (NSps) is identical in all directions, resulting in a single LSPR absorption peak (**Figs. 7A** and **B**) [88]. When the shape of Au changed to nanorods (NRs), it exhibited two LSPR absorption peaks corresponding to plasmonic resonance in longitudinal and transverse directions [88], as shown in **Figs. 7C** and **D**. Moreover, the longitudinal LSPR absorption of Au NRs located at a longer wavelength is broader and much higher in intensity than that of the Au nanospheres. For the Au NRs with different aspect ratios, even though absorption spectra contain two absorption peaks corresponding to the separate plasmonic resonances in the transverse and longitudinal directions, the peak position and absorption intensity can also be well-tuned by simply modulating the aspect ratio of Au NRs [84]. A broader spectral range of the light source of Au NRs is beneficial for making full use of light, thus contributing to the enhanced photocatalytic performance of Au-based composite. Next to NSps and NRs, the shape of Au can also be triangular, spheroid, cubes, pentagon, ellipsoid, nanoshell and even irregular [84], in which various morphologies generally have multiple resonant peaks due to the multipolar resonances in different directions.

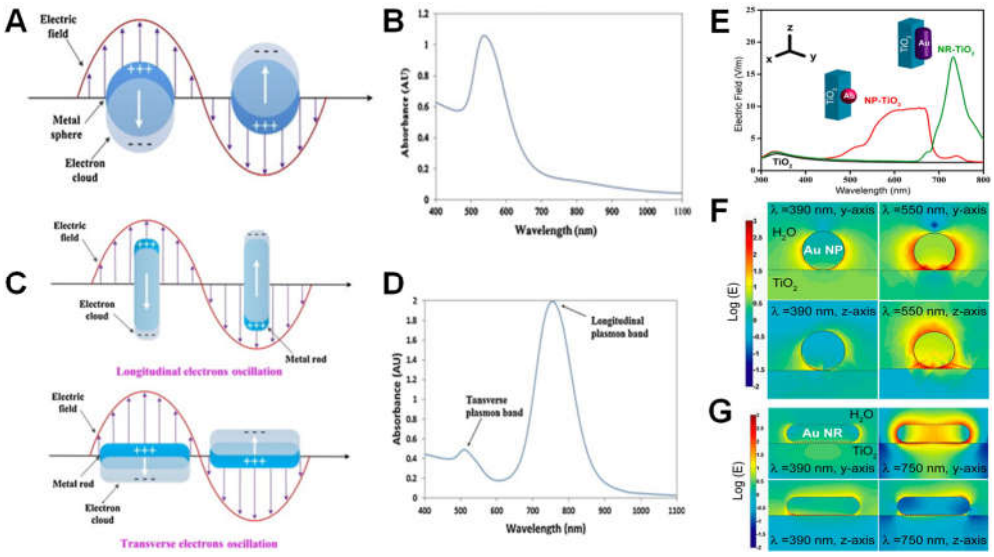

Fig. 7. (A-D) Schematic illustration of plasmonic resonance and typical LSPR absorption peak for (A and B) Au nanospheres and (C and D) nanorods. Reproduced with permission from ref. [88]. Copyright 2014, Elsevier. (E-F) Spatial distribution of electric field on the y-z plane for Au NP-TiO_2 and Au NR-TiO_2. Reproduced with permission from ref. [90]. Copyright 2013, American Chemical Society.

In addition to the LSPR absorption peak, the morphology of Au NSs affects the near-field enhancement. Based on theoretical analysis, Kumarasinghe et al. reported that electron generation and injection of Au NRs were several orders of magnitude higher than those of NSps with similar volume due to the stronger near-field enhancement [89]. Pu et al. recently studied the effect of Au shape on the near-field effect using an Au-decorated TiO_2 sample. Their results showed that the spherical Au decorated TiO_2 provides an enhancement of the near field on the order of 5 times compared to the applied field while this enhancement is 15 times in the case of Au NRs (**Figs. 7E** and **F**) [90].

Following these reports, the impact of Au morphology on both optical property and near-field enhancement and ultimately photocatalytic performance have been examined. For instance, Guo et al. investigated the role of Au shape (NSps and NRs) on photocatalytic H_2 evolution over Au/graphitic carbon nitride (g-C_3N_4) [91]. After 3 h of visible light irradiation, the optimal H_2 production rates over Au NRs/g-C_3N_4 reached around 510 μmol g^{-1} h^{-1}, which was about 1.5-fold higher than that of Au NSps-based (350 μmol g^{-1} h^{-1}) samples. Optical and photoelectrochemical measurements showed that the enhanced activity was attributed to (1) efficiently endowing the hybrid photocatalysts with an extended light absorption range compared to Au NSps; (2) Au NRs promoted the separation of electron-hole pairs more efficiently than Au NSps. Similar results have also been confirmed by Pap et al., who investigated the relationship between different geometries of Au NSs (wire, triangle and sphere) and photocatalytic H_2 evolution performance [92]. After 120 min UV irradiation, the highest H_2 production rate was achieved on the Au NSps-TiO_2 sample. Detailed analyses indicated that the modification of Au NSps can dramatically change the optical properties of Au (i.e., electron transition bands), thus leading to enhanced photocatalytic performance toward H_2 generation. Besides NSs and NRs, Au with other morphologies (nanoplates, nanostar, and faceted nanocrystals) decorated Cu_2O [93], ZnO [94], CdS [94], $ZnIn_2S_4$ [95], etc., have been developed for solar to fuel conversion, further confirming that the photoactivity greatly associated with the shape of Au NSs.

Furthermore, the Au shape-based near-field enhancement has been investigated theoretically and experimentally, and the photocatalytic performance of the Au-based composite is shown to be highly related to the near-field effect [72]. Up to now, the effect of the near-field enhancement on various morphologies of Au NSs (NSps, NRs, nanostar, triangle, nanocube) decorated semiconductor systems, such as $SrTiO_3/TiO_2$

[96], C_3N_4 [97], ZnO [98], Cu_2FeSnS_4 [99] for H_2 generation and CO_2 reduction have been widely reported. These studies confirm that the shape of Au NSs induced near-field enhancement has a big influence on photocatalytic activity. This is because the strong near field simultaneously enables LSPR energy transfer processes such as hot electron injection, and even dipole-dipole coupling, thus effectively enhancing electron generation and injection, and ultimately boosting the solar-to-fuel conversion [72]. Note that when comparing the photocatalytic performance with different Au morphologies, the effect of size should be ruled out since size also directly affects the final photoactivity, which will be discussed in section 4.2.

Overall, Au NSs possess unique LSPR effects and hold particular strengths in enhancing incident light trapping and extending the optical response range across the full solar spectrum [100]. The integration of Au into semiconductor supports, through controlling the morphology/shape of Au NSs, offers huge opportunities to maximize the utilization of solar energy and improve the conversion efficiency of solar energy into available chemical energy [101-103]. However, although some studies intentionally control the shape for solar fuel production using Au-based photocatalysts, the underlying benefits of Au NSs are still under debate. Taking Au NSps and NRs as examples, some researchers reported that the Au NSps modified semiconductor composite exhibits better photocatalytic performance compared to Au NRs-based sample [92, 93]. while others showed that superior performance is achieved on Au NRs [91, 98]. Therefore, understanding the exact role of Au morphology in promoting the performance is of crucial importance for designing Au-based photocatalysts with high efficiency toward solar-to-fuel conversion.

4.2 Controlling size

In parallel with the shape, the size of Au NSs can be tuned in a large range from nanoparticles to nanoclusters and single atoms level. The size of Au NSs directly contributes to the LSPR phenomenon and the energy transfer processes under light irradiation [72], thus exerting an influence on the photocatalytic performance of Au-semiconductor composite photocatalysts. Regarding the Au nanoparticles, Wang and coworkers reported that the size increment of Au NSps leads to a red-shift in the LSPR due to a low frequency for the collective oscillation of electrons, which causes electromagnetic retardation [73, 104]. Yamada et al. showed that the Au NSps have a strong LSPR absorption maximum at around 520 nm when the size is in the range of

10 nm;[105] while it changes to 520-530 nm as size reaches 10-40 nm, and LSPR peak moves to 530-580 nm with further increase the size to 40-100 nm (**Fig. 8A**) [106]. Note that the size of Au NSs is critical for hot electron generation and injection. The Au NSs with large sizes are reported to produce a larger number of hot carriers since a red-shifted LSPR peak as the size increases enable a higher harvest efficiency of visible and near-infrared light [87, 106]. Contrarily, smaller Au NSs render fewer charge carriers than the large ones, while the generated electrons from small Au NSs generally possess higher energies, which could overcome the Schottky barriers between Au and semiconductor more easily [69, 87]. Thus, two different conclusions were drawn regarding the influence of Au size on photocatalysis.

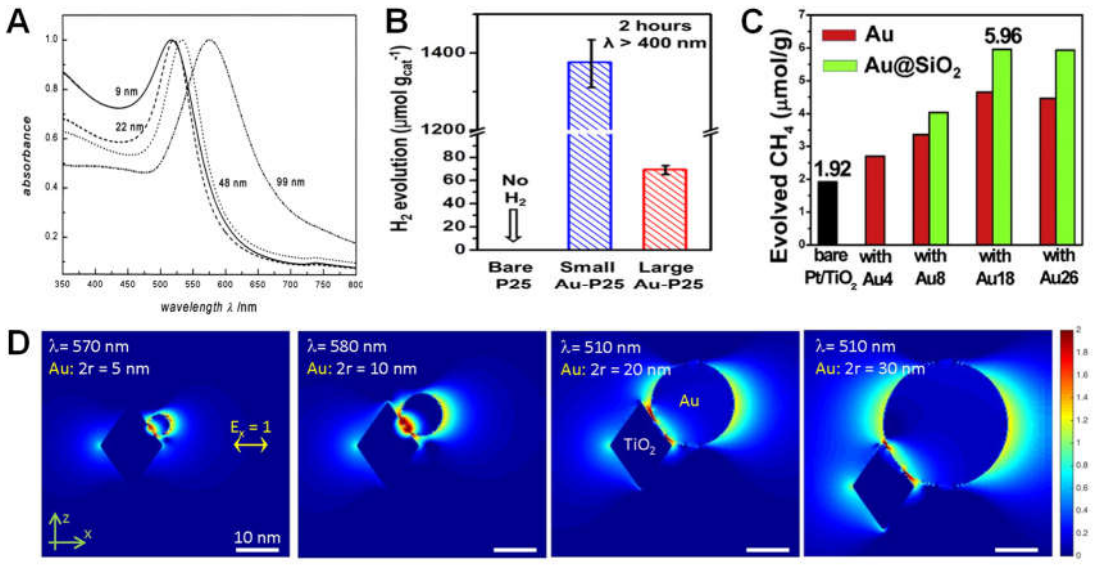

Fig. 8. (A) UV-vis absorption spectra of Au NSs with different sizes. Reproduced with permission from ref. [106]. Copyright 1999, American Chemical Society. (B) Photocatalytic H_2 generation over Au-P25 with small Au and large Au NSs. Reproduced with permission from ref. [107]. Copyright 2014, American Chemical Society. (C) photocatalytic CO_2 conversion to CH_4 over $Pt/TiO_2/Au@SiO_2$ photocatalysts with the with various Au sizes. Reproduced with permission from ref. [108]. Copyright 2016, Elsevier. (D) Simulated light intensity enhancement for the different sizes of Au on TiO_2 at the wavelength, Reproduced with permission from ref. [109]. Copyright 2017, Elsevier.

More specifically, some studies showed that the decrease of Au NSs size favors photocatalytic conversion of solar energy into fuel over Au-semiconductor composite [107, 110]. For example, the H_2 generation over Au/TiO_2 composites with different

sizes of Au was studied by Wei's group [107]. Under visible light irradiation ($\lambda > 400$ nm), the small Au-TiO_2 sample (4.4 nm) showed an H_2 generation rate of 1376 μmol g^{-1} (**Fig. 8B**), which was about 20 times higher than that of large Au-TiO_2 (67 nm) with an H_2 production rate of 69.4 μmol g^{-1}. The enhanced photoactivity was explained as follows: compared to large Au NSs, the smaller ones induce a greater negative shift in the Fermi level, and then enable a better charge separation and suppressed recombination of electron-hole pairs. Photoluminescence spectroscopy further provided evidence for better charge separation within the smaller Au-TiO_2 sample as compared with that of larger Au-TiO_2. Following this work, Teranishi et al. reported that decreasing the size of Au NSs will diminish the density of states [110], increase the entropic driving force for the hot-electron injection from Au to TiO_2, and simultaneously reduce the back electron transfer. The charge separation is consequently improved with a long lifetime of electron-hole pairs, leading to boosted photocatalytic performance.

On the contrary, some studies indicated a positive effect on electron generation and injection as the increase in Au NSs size, and ultimately the improved photoactivity [72, 108]. For instance, Bera et al. investigated the photocatalytic CO_2 conversion over Pt/TiO_2/Au@SiO_2, where the sizes of Au nanoparticles varied from 4 to 26 nm [108]. The catalytic activity in evolving CH_4 reached about 6 μmol g^{-1} for Au with the size of 26 nm (**Fig. 8C**), which was a 1.5-fold enhancement compared to 8 nm Au NSs (4.03 μmol g^{-1}). The enhanced photoactivity is attributed to the reduction potential of injected hot electrons, where large Au NSs enable efficient electron injection to the nearby TiO_2 whereas small ones suffer from a low injection efficiency of hot electrons [107]. A similar phenomenon was also observed by Vu et al. [72], who reported that a large size of Au allows electron accumulation in the CB of TiO_2, which manipulates the reduction potential of those electrons and thus facilitates the photocatalytic process. Moreover, the local electric field enhancement is strongly dependent on the size of Au NSs [72, 111]. For instance, Li et al. reported that as the Au size increased from 5 to 30 nm, the local electric field around Au NSs will gradually enhance, leading to an increased number of hot electrons and thus affecting the final photocatalytic activity (**Fig. 8D**) [109]. When these Au NPs were applied to the photoreduction of CO_2 over Au/C_3N_4 photocatalysts, the optimal CO yield was 80.8 μmol g^{-1} with the Au size of 20 nm, which was over 2.5 times greater than that of small-size Au decorated C_3N_4 (32.6 μmol g^{-1}). Beyond C_3N_4, changing Au sizes to tuning the local electric fields of Au/TiO_2

[109], Au/$BiVO_4$ [112], Au/ZnO [72] was also reported to promote the photocatalytic solar-to-fuel conversion efficiency. Note that a consensus has not been reached yet regarding the size effect of Au on regulating the final photocatalytic performance of Au-based composite. The above discussion suggests that the size-related multi-functional roles of Au NSs, including size-related hot electron generation and injection, local electric field enhancement of Au NSs and charge transfer dynamics between Au and semiconductor, should all be taken into consideration when comparing the performance of different Au-based photocatalysts.

On the other hand, since only the exposed Au atoms participate in the redox reactions [8], to minimize the waste of the non-accessible atoms, downsizing the size of Au NSs to the atomic level is a promising method to further improve their catalytic efficiency [113]. In recent years, the design of Au clusters and single atoms based catalysts for photocatalysis has attracted much attention (**Fig. 9A**) [114]. Besides the accessible atoms, significant changes occurred in both electronic structure and optical properties once the size of Au decreased from nanoparticles to clusters or single atoms, which could increase the light-harvesting ability, accelerate charge transfer dynamics, and enhance the absorption and activation of reactants, thus contributing to the photoactivity enhancement [8, 115].

Specifically, Au clusters have been exploited to boost photocatalytic solar-to-fuel conversion performance. For example, Xiong's group reported that efficient visible-light-induced CO_2 reduction with an electron consumption of 31.1 μmol g^{-1} h^{-1} was achieved through tuning Au clusters catalytic active cites, in which metal cations such as Ni^{2+} were grafted to Au cluster using l-cysteine as a bridging ligand [116]. Similarly, Wang et al. investigated the role of Au clusters (*ca.* 1.65 nm) during photocatalytic CO_2 reduction [117]. *In-situ* DRIFTS results showed that the Au clusters-TiO_2 composites effectively suppress the CO adsorption compared to Au nanoparticles-TiO_2 samples, attributing to the electron-rich state of Au clusters, and the under-coordinated Au ensures the more efficient $^*H$ production from the H_2O splitting. Besides, physical and electronic characterizations indicated that the electronic interaction between Au clusters and TiO_2 support is stronger than that in Au nanoparticles-TiO_2 interface. As a result, after 0.5 h of UV light irradiation, the Au clusters/TiO_2 sample produced CO and CH_4 of 8.77 and 3.92 μmol g^{-1} h^{-1}, respectively, which is slightly higher than the Au nanoparticles-TiO_2 composite (7.52 and 3.57 μmol g^{-1} h^{-1} for CO and CH_4, respectively), as shown in **Fig. 9B**. Similar results were also observed in Au@COF

[118], Au@C_3N_4 [119], and Au/ZnO [120] photocatalytic systems. Recently, an impressive H_2 production rate of 404 μmol h^{-1} (**Fig. 9C**) over Au cluster modified CdS composite was reported by Shen et al. [121], where the average size of Au clusters was about 0.95 nm, leading to an 11 times enhancement compared to the sample with 9 nm Au.

Despite considerable research attention have been paid to design Au clusters modified semiconductor photocatalysts, the Au clusters under light irradiation generally suffer from serious instability and tend to aggregate into large Au nanoparticles, which leads to reduced photocatalytic performance, thus hampering their wide and large-scale applications [16, 66, 122]. Therefore, developing stable and efficient Au clusters-based composites to avoid their aggregation is fundamentally important for photocatalytic solar-to-fuel conversion while the research work in this area is still less.

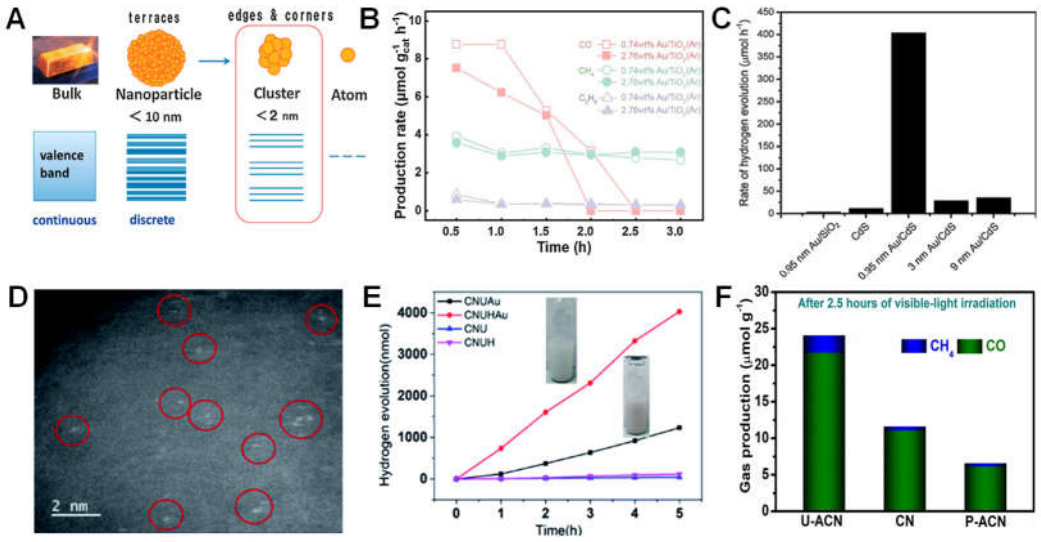

Fig. 9. (A) Schematic illustration of electronic structures of bulk, nanoparticle, cluster, dual atom, and single atom of Au metals. Reproduced with permission from ref. [114]. Copyright 2014, Chemical Society of Japan. (B) Production rate of CO_2 reduction over Au cluster/TiO_2 photocatalysts. Reproduced with permission from ref. [117]. Copyright 2021, Elsevier. (C) H_2 evolution rates over Au/CdS with different sizes of Au clusters. Reproduced with permission from ref. [121]. Copyright 2012, Elsevier. (D) Aberration-corrected scanning transmission electron microscopy image of single Au atoms on the surface of g-C_3N_4. (E) Photocatalytic H_2 generation over CNUHAu and other samples under visible light irradiation. Reproduced with permission from ref. [123]. Copyright 2019, Royal Society of Chemistry. (F) Photocatalytic CO_2 reduction over Au single atoms/U-ACN, CN, and Au/P-CAN photocatalysts. Reproduced with permission from

ref. [124]. Copyright 2020, Wiley-VCH.

Beyond the Au clusters, decreasing the size of Au to the single-atom level has been believed to further expose its surface atoms and attracted considerable research attention recently for photocatalytic solar-to-fuel conversion [123, 124]. For instance, the Xue group reported the single atom Au incorporated graphitic carbon nitride (CNUH) for photocatalytic H_2 generation (**Fig. 9D**) [123]. After 5 h of visible light irradiation, CNUH/Au exhibited an H_2 generation rate of 789.1 nmol h^{-1} (**Fig. 9E**), much higher than that of pure CNUH photocatalyst (48.9 nmol h^{-1}). Following this report, single atom Au decorated TiO_2 (such as defective TiO_2 with vacancies) [125, 126], C_3N_4 [127], $Cd_{1-x}S$ [128], and MOFs [129] with improved H_2 generation rates have also been adopted in the past few years.

Next to photocatalytic H_2 evolution, the Au single atoms based photocatalysts are employed for CO_2 reduction. For example, Yang et al. synthesized an Au single atoms decorated amino-modified graphitic carbon nitride photocatalyst (U-ACN) [124]. After 2.5 h of visible light irradiation, the U-ACN showed yields of 21.7 and 2.4 μmol g^{-1} for CO and CH_4, respectively, which were about 4 times higher than the carbon nitride counterpart **(Fig. 9F)**. Recently, Si et al. reported that low-coordination single Au atoms (Au_1-S_2) on $ZnIn_2S_4$ nanosheets not only promote charge transfer to underpin its superior photoactivity for CO_2 reduction but also greatly reduce the energy barrier for protonation of $^*CO$ and stabilize the $^*CH_3$ intermediate, thereby leading to the selective CH_4 generation during CO_2 photoreduction [130]. Beyond these reports, single atomically dispersed Au on CdS (with or without vacancy) [131], MoS_2 [132] and red phosphorus [133] supports have been reported and investigated symmetrically for photocatalytic CO_2 reduction.

To sum up, the size of Au NSs has been demonstrated to play a vital role in determining the photocatalytic performance for solar-to-fuel conversion under light irradiation. The change in Au sizes significantly affects their physical and chemical properties, which alters their roles in promoting the photoactivity of Au-based composite. Note that when the sizes of Au NSs are too large, they may serve as electron-hole recombination sinks [8, 72]; while reducing the Au NSs size too much could completely dampen their plasmonic effect [72]. Additionally, the heating effect in Au NSs scales quadratically with the radius, in which larger Au NSs are more prone to decay radiatively, thus reducing the amount of locally dissipated heat [87, 134].

Therefore, those factors simultaneously contribute to the photocatalytic performance of Au-based composite, which leads to the debate regarding the size-dependent photoactivity toward solar-to-fuel conversion, while an in-depth insight into the understanding of detailed reaction mechanism is still lacking.

Besides, although considerable research attention have been paid to single Au atom-modified semiconductor photocatalysts, their applications in solar-to-fuel conversion are in the fancy stage [8]. Moreover, there are still many challenges that need to be addressed for Au single atoms based photocatalysts, including developing easy and effective methods for the synthesis of Au single atoms, pursuing suitable strategies to synthesize composites with high loading of Au single atoms, and exploring deployable solutions to achieve long-term stability [135]. Additionally, the photocatalytic performance of Au single atoms based photocatalyst is still unsatisfactory. Therefore, developing more effective approaches is anticipated to move the Au-based photocatalysts for solar-to-fuel conversion forward.

4.3 Engineering phase and defect

Au NSs with different crystal phases and certain defects possess different physicochemical properties due to the different atomic arrangements and modified electronic structures [39, 42, 136]. Generally, the vast majority of reported Au NSs exhibit the traditional face-centered cubic (fcc) structure, while Au NSs with various phases, such as body-centered cubic (bcc), hexagonal close-packed (hcp), have been reported theoretically and experimentally (**Fig. 10A**) [136]. These various phases of Au NSs have been demonstrated to ultimately affect the photocatalytic solar-to-fuel conversion efficiency of Au-based photocatalysts.

For instance, Zhou et al. reported that a longer charge carrier lifetime was achieved by engineering the crystal phase of Au nanoclusters [137], where the bcc-structured Au_{38} nanoclusters have a longer excited state lifetime than the fcc nanoclusters, which is beneficial for the separation/migration of charge carriers and the catalytic performance. Over the past few years, Zhang's group experimentally developed Au NSs with different phases, such as hcp (2H and 4H phase) [43, 44, 138, 139]. In recent work, they investigated the photocatalytic dimerization of *para*-nitrothiophenol under visible light on unconventional 4H Au and conventional fcc phases [140]. The results showed that the reaction proceeded over 4H Au was about 8 times that of fcc Au counterpart. Although the advantages of phase-engineered Au NSs have been proved in

electrocatalysis or single Au driven photocatalysis, so far, the coupling of these Au NSs with semiconductors for solar-to-fuel conversions, such as photoreduction of CO_2 and H_2 generation, has rarely been reported. Therefore, further applications can be expected in the field of photocatalysis through rational design of engineering Au phase, and it may bring the next breakthrough in Au-modified photocatalysts.

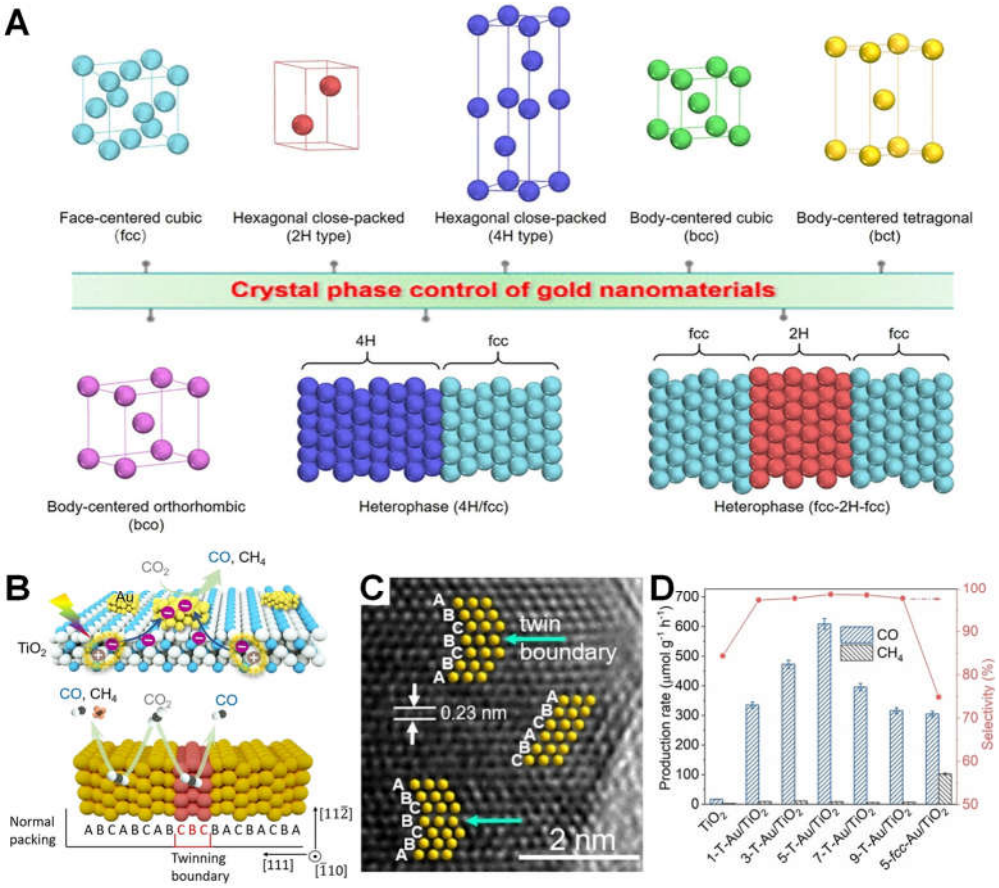

Fig. 10. (A) Schematic representation of different crystal phases and heterophase of Au NSs. Reproduced with permission from ref. [136]. Copyright 2020, American Chemical Society. (B) Schematic illustration of photocatalytic CO_2 reduction over conventional fcc-Au/TiO_2 (top) and twinned Au/TiO_2 (bottom) photocatalysts. (C) High-resolution transmission electron microscopy image with the scheme of twin boundary Au. (D) Photocatalytic performance of CO_2 reduction over TiO_2, a series of twinned Au/TiO_2 and fcc-Au/TiO_2 photocatalysts. Reproduced with permission from ref. [64]. Copyright 2022, Wiley-VCH.

Next to the phase, engineering defects on Au NSs is another promising approach for boosting the photocatalytic performance in solar-to-fuel conversion. Especially, the twinning boundary in Au NSs has been reported to improve the electrical properties and

thereby contribute to photoactivity enhancement [141-143]. A recent work by Weng et al. investigated the effects of the twinning boundary of Au nanoparticles (T-Au) on selective reduction of CO_2 to CO over Au/TiO_2 samples (**Fig. 10B**), in which the as-formed T-Au was confirmed by HRTEM (**Fig. 10C**). Theoretically, the differences in the thermodynamics and reaction pathways for CO_2 reduction over fcc-Au and T-Au were examined. The calculation results showed that T-Au was more favorable for the desorption of CO molecules and protonation of *CO to produce *COH, originating from the significant change in the adsorption configuration of *COOH intermediate on the T-Au surface. As a result, the CO yield over T-Au/TiO_2 was elevated to 608 μmol g^{-1} h^{-1} with a 99% CO selectivity after 4 h of solar light illumination, while the fcc-Au/TiO_2 sample generated 305 μmol g^{-1} h^{-1} of CO and 102 μmol g^{-1} h^{-1} of CH_4 (**Fig. 10D**), suggesting that T-Au NSs can effectively improve the CO selectivity.

Although this work showcases the engineering of twin defect on Au NSs for controlling the selectivity of CO_2 reduction, defect engineering on Au NSs has not been fully exploited compared to other semiconductors (TiO_2, $Cd_{1-x}Zn_xS$, CuS, etc.). Besides, it is still challenging to precisely tune the ratio between the twin and routine boundaries of the Au NSs. In addition, the benefits and the difference regarding the introduction of twins to different morphologies of Au NSs systems have not been investigated. Therefore, there is still plenty of room to be exploited.

4.4 Alloying with different metals

Compared to single Au NSs, the construction of Au alloys has been shown to greatly alter their LSPR properties, which can expand the light response range and influence the charge dynamics, thereby improving the photocatalytic performance of Au-based composite [71]. Meanwhile, the LSPR properties of Au-based bimetallic alloys are revealed theoretically. For example, Chao et al. showed that the unique optical response of alloys is related to the existence of an LSPR mode at the interface [144], and the physical origin of the unique LSPR feature is associated with the LSPR peak shift and local field distribution near their surfaces. Taking Au@Pt and Au@Pd as examples, the LSPR of both structures can occur in the visible region with broad tunability, which could benefit the enhancement of the photocatalytic properties of Au [144]. Moreover, Au alloys are beneficial for the adsorption and/or activation processes of reactants, improving the selectivity of products, etc. [71, 145], Additionally, alloying the Au with

non-noble metals (such as Ni, Cu) offers a useful route to simultaneously increase photoactivity and decrease the cost of the catalysts compared to single Au NSs [73].

Generally, five groups of alloys can be identified depending on the physical form of the metals, i.e., ordered, random, core-shell, sub-cluster segregated, and multi-shell alloys (**Fig. 11A)** [146]. So far, many types of Au-based alloys, such as Au-Pt [147, 148], Au-Ag [149, 150], Au-Pd [151, 152], Au-Cu [153, 154], and Au-Ni [155, 156], have been developed and studied for photocatalytic solar-to-fuel conversion.

Experimentally, Song et al. loaded Pt-Au alloys onto the surface of SiO_2 to study the effect of alloys on photocatalytic CO_2 reduction under solar light irradiation [157]. The intensities of electric fields on Pt-Au/SiO_2 at 530 nm were significantly higher than that of Au/SiO_2, originating from the strong near-field coupling between Pt and Au. The generated strong electric fields yielded high concentrations of hot electrons, making the Au surface sites more active for CO_2 reduction. Moreover, hot electrons generated from Pt-Au alloys transfer to the adsorbed CO_2 and intermediate $COOH^*$ and CO^* species to weaken the chemical bonds (**Fig. 11B**), the lower surface coverage of adsorbed CO* and $COOH^*$ species, and accelerate the desorption of CO and H_2, resulting in the reduction of activation energy for photocatalytic CO_2 reduction. As a result, under solar light illumination, the CO yield over Pt-Au/SiO_2 reached 125 μmol g^{-1} min^{-1} (**Fig. 11C**), which was about 10-fold higher than that of the Au/SiO_2 counterpart. A similar result was also demonstrated by Xue et al. [158]. They prepared Au-Pt alloys decorated TiO_2 photocatalyst for CO_2 reduction under UV-vis light irradiation. The optimized Au/Pt/TiO_2 catalyst exhibited 2.4 times higher activity in CH_4 production (0.57 μmol h^{-1}) than the Au/TiO_2 sample. Recently, the decoration of Pt-Au alloys on Al_2O_3 [159], TiO_2/$NaTaO_3$ [160], $CaIn_2S_4$ [161], WO_3 [162] supports has been used for various photocatalytic solar-to-fuel reactions. Overall, the enhanced photocatalytic activities could be attributed to the synergy of an electron-sink function of Pt and Au LSPR effect that improves charge separation and provides more reaction sites.

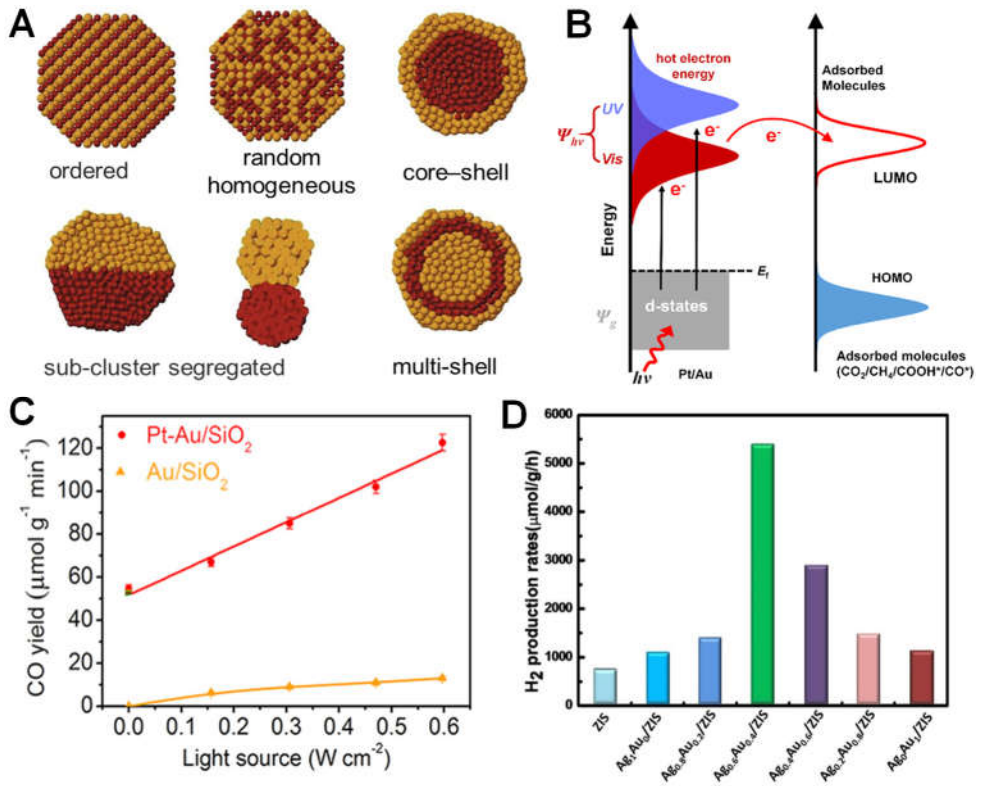

Fig. 11. (A) Schematic representation of five typical mixing patterns of Au-based bimetallic alloys. Adapted with permission from ref. [146]. Copyright 2020, Elsevier. (B) Schematic illustration of energy transfer from photoexcited plasmon states to molecular states within Pd/Au. (C) CO yield over Au/SiO_2 and $Pt\text{-}Au/SiO_2$ under various light intensities. Adapted with permission from ref. [157]. Copyright 2017, American Chemical Society. (D) H_2 production rate over $Ag_xAu_{1-x}/ZnIn_2S_4$ photocatalysts (ZIS: $ZnIn_2S_4$). Reproduced with permission from ref. [163]. Copyright 2019, Elsevier.

In addition, by merely adjusting the Ag-Au composition, the optical absorption properties of Ag_xAu_{1-x} alloys could be tunned significantly, in which the absorption band of alloys was controllable within a wavelength window of 80 nm [163]. When applying this composite system to the H_2 generation reaction, an optimal H_2 production rate of 5400.7 μmol g^{-1} h^{-1} over $Ag\text{-}Au/ZnIn_2S_4$ was obtained, which was approximately 5-fold enhancement compared to $Au/ZnIn_2S_4$ (1131 μmol g^{-1} h^{-1}) sample (**Fig. 11D**). In-depth analysis showed that when introducing the Ag-Au alloys onto the $ZnIn_2S_4$ surface, this system has two advantages: (1) the maximum optical absorption achieved by the combination of $ZnIn_2S_4$ with Ag_xAu_{1-x} leads to the generation of more electrons; (2) the efficient separation of electrons and holes in

$ZnIn_2S_4$ resulted in prolonged charge carrier lifetime since the Schottky barrier height formed between Ag_xAu_{1-x} and $ZnIn_2S_4$ interface was adjusted. Following this concept, coupling the Ag-Au alloys with other semiconductors such as g-C_3N_4 [164], SiO_2@TiO_2, [165] ZnO/CdS [166], and Au-Pd alloys attached on TiO_2 [167], $NaTaO_3$ [168], $ZnIn_2S_4$ [169], have been reported to enhance the photocatalytic performance of H_2 generation and CO_2 reduction under light irradiation.

The above examples show the benefits of alloying Au with noble metals. While considering the scarcity and high cost of precious metals, it is meaningful to explore non-noble metal alternatives. Metals Cu, Ni et al. are reported to simultaneously guarantee the advantages of Au-metal alloys and reduce the overall cost [153-156]. For example, Liu et al. showed that besides shutdown of the cost [153], alloying of Cu into Au nanoparticles causes a distinct increase of inter-band transition intensity (ca. 525 nm) over Au-Cu alloys, and a red shift of SPR absorption was observed compared to that of pure Au. Besides, the restraint of Cu oxidation in Au-Cu alloys modified the electron transfer direction between Au and Cu on the surface, enabling effective metal photosensitization. After 6 h of visible light irradiation, the Au-Cu/$SrTiO_3$ sample exhibited an H_2 evolution activity of 29.5 μmol g^{-1} h^{-1}, which was 1- and 4.5-fold higher than the Au/$SrTiO_3$ and the mechanical mixed Au and $SrTiO_3$ samples, demonstrating the synergistic effect of the as-formed Au-Cu alloy in promoting H_2 evolution. Similarly, Au-Cu alloys supported on $SrTiO_3$/TiO_2 [154], TiO_2/MoS_2 [170], CuS/TiO_2 [170] are developed for photocatalytic solar-to-fuel conversion. In parallel with Cu, Au-Ni decorated on TiO_2 [155], g-C_3N_4 [156], SiO_2 [171], and Au-Co attached on TiO_2 [172], C_3N_4 [173, 174], have been adopted for photocatalytic H_2 generation or/and CO_2 reduction. These studies indicate a feasible route to improve the photocatalytic processes driven by noble metal, with non-precious metals, in Au-based alloys modified semiconductor composites toward solar-to-fuel conversion.

To summarize, alloying Au with different metals has attracted much attention in the field of photocatalysis since the synergistic effect of Au and other metals can further improve the activity. Besides the bimetal, tailoring the composition of Au-based alloy nanometals may become a rising research hotspot. High-entropy alloys are of great research interest in materials science and engineering [175, 176]. Unlike conventional alloys which normally contain two elements, high-entropy alloys comprise multiple principal elements, with great advantages such as excellent specific strength, superior mechanical performance, exceptional ductility and fracture toughness,

superparamagnetic, and superconductivity [175]. Due to their considerable structural and functional potential as well as the richness of design, Au-based high-entropy alloys are an interesting candidate for further enhancing the photocatalytic solar-to-fuel conversion efficiency of Au-based composite catalysts.

4.5 Modulating interfacial interaction

Interface engineering is an effective approach to mediate the near-range coordination and electronic interaction between Au NSs and semiconductors [177]. Considering the interface between two components is the location for charge transfer and separation, the interface parameters, including interfacial compositions, facets, and band bending greatly influence the charge transfer and separation efficiency [178]. Subsequently, these interfacial parameters determine the photocatalytic solar-to-fuel conversion efficiency and selectivity since they affect the surface reactive sites, adsorption, and activation abilities. Given that, the effect of the junction states of Au-semiconductor hybrids, such as suitable interface and the accessible area between each component (**Fig. 12A**) and charge redistribution (**Fig. 12B**), has been studied [179-182] Accordingly, the rational interface design can achieve a high photocatalytic performance of Au-based composites.

Hung et al. reported that the charge transport interface between Au and TiO_2 nanotube can be tuned by controlling the Au core and Pt shell structure, where the Au@Pt enables both semiconductor/Au and Au/electrolyte interfaces for efficient H_2 evolution [179]. Next to the LSPR effect originating from the Au, the engineered interface presented a synergistic effect, which not only lowers the Schottky barrier on the interface, but also offers sufficient kinetics for proton reduction. As a result, an H_2 generation rate of about 3 mmol g^{-1} h^{-1} was achieved over TiO_2-Au@Pt hybrid after solar light irradiation for 6 h, showing a significant enhancement compared to Au-TiO_2 (1.4 mmol g^{-1} h^{-1}) (**Fig. 12C**). This work demonstrated that the mediation of the Au/TiO_2 interface was beneficial for improving the electron transfer and adjusting the H_2 evolved kinetics, thus improving the H_2 generation rate. In addition, Madhusudan et al. proved that by engineering the Au in an all-solid-solid Z-scheme system ($Zn_{0.5}Cd_{0.5}S$/Au@g-C_3N_4) [180], the charge transport interface between Au and semiconductors can be maximized, thus enhancing the photocatalytic performance of CO_2 reduction under visible light illumination.

Besides, engineering the interfacial facet between the Au and semiconductor has

been adopted to enhance photocatalytic performance [181]. This is because different exposed facets exhibit unique electronic band structures, and band alignment, which affects the Schottky barrier between metal Au and semiconductor [183]. Specifically, Wang et al. decorated Au onto the surface of TiO_2 with dominant (001) and (001) facets for photocatalytic CO_2 reduction under ultraviolet and visible light irradiation [181]. A significant enhancement in the photocatalytic activity was achieved by Au-TiO_2(101) (CO: 25.9 μmol g^{-1} h^{-1}, CH_4: 5.3 μmol g^{-1} h^{-1}) as compared to Au-TiO_2(001) (16.5 and 4.0 μmol g^{-1} h^{-1} for CO and CH_4, respectively) (**Fig. 12D**). In-depth analysis indicated that the formation of the Au/TiO_2(101) interface exhibited a lower Schottky barrier height than the Au/TiO_2(001) sample, which is favorable for the transfer of the electrons from TiO_2 to Au under light irradiation (**Fig. 12E**). Generally, the more efficient interfacial charge transfer and separation, the more electrons can participate in the photocatalytic process [18]. Thus, the Au/TiO_2(101) sample significantly improves the photocatalytic activity for CO_2 reduction.

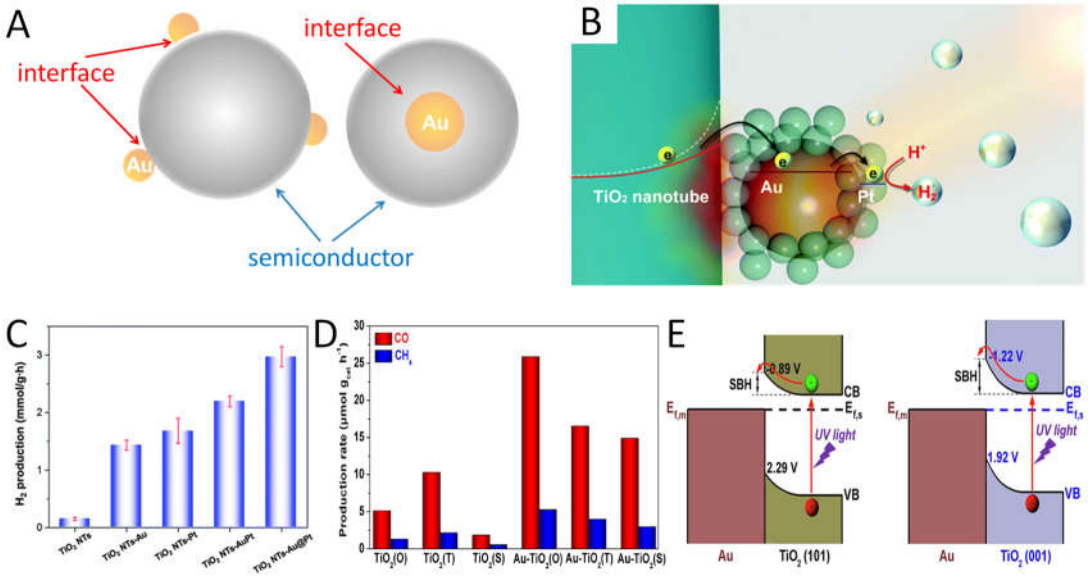

Fig. 12. (A) Schematic representation of the typical interface in Au/semiconductor composites. (B) Interface engineering through the introduction of another metal (Pt) to modulate the interface between Au and semiconductor (TiO_2). (C) Photocatalytic performance of H_2 generation over TiO_2/Au@Pt composites under solar light irradiation. Reproduced with permission from ref. [179]. Copyright 2016, Royal Society of Chemistry. (D) The production rates of CO and CH_4 from photoreduction CO_2 over Au-TiO_2 materials under UV light illumination. (E) Schematic representation of the electron transfer behaviors originating from the band alignments between Au and TiO_2 with different facets. Reproduced with permission from ref. [181]. Copyright 2020,

Elsevier.

Apart from the Schottky barrier height, balancing the contact surface area between Au NSs and semiconductors to tune the localized electric field has been proven to be vital for boosting photocatalytic solar-to-fuel conversion performance. For instance, Ha et al. synthesized two distinct morphologies of Au (spherical (Au_{sp}) and multipod (Au_{mp}) and incorporated them onto Cu_2FeSnS_4 support for investigating the influence of contact surface area on photoactivity [99]. When applied to photocatalytic H_2 generation reaction, the Au_{mp}/Cu_2FeSnS_4 sample displayed an improved photoactivity (90 μmol g^{-1} h^{-1}) compared to Au_{sp}/Cu_2FeSnS_4 (59.5 μmol g^{-1} h^{-1}) (**Fig. 13A**). Although the contact surface area between Au and Cu_2FeSnS_4 in Au_{mp}/Cu_2FeSnS_4 composite was estimated to be around one-half in Au_{sp}/Cu_2FeSnS_4, the increased size and anisotropic shape of Au_{mp} could generate a more intense localized electric field under light irradiation, thus contributing to the photoactivity improvement. Similarly, Patnaik et al. reported a defective surface of g-C_3N_4 to benefit the adsorption of Au nanoparticles on the oxygen vacancies for improving the extent and effectiveness of the electronic communication between Au and g-C_3N_4 [182]. Accordingly, the photocatalytic H_2 evolution activity over Au-sulfated g-C_3N_4 is about 35-fold higher than that of g-C_3N_4 under visible light irradiation (**Fig. 13B**).

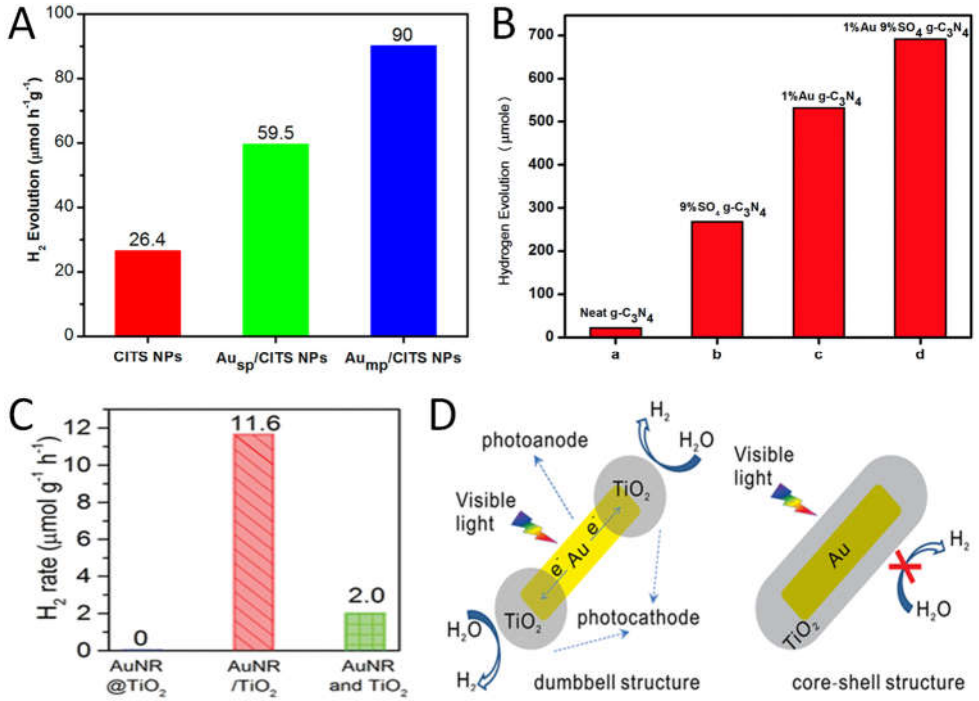

Fig. 13. (A) Photocatalytic performance of H_2 generation over CITS, Au_{sp}/CITS, and Au_{mp}/CITS core@shell nanomaterials under visible light irradiation. Reproduced with

permission from ref. [99]. Copyright 2015, American Chemical Society. (B) H_2 yield over pure g-C_3N_4, SO_4 g-C_3N_4 and Au decorated composites. Reproduced with permission from ref. [182]. Copyright 2016, Owner Societies. (C) H_2 generation rate over AuNR@TiO_2, AuNR and TiO_2, and AuNR/TiO_2 photocatalysts. (D) Schematic illustrating the reaction mechanisms with AuNR/TiO_2 dumbbell and core/shell AuNR@TiO_2 structures. Reproduced with permission from ref. [184]. Copyright 2016, American Chemical Society.

Generally, coating Au NSs with semiconductors to form a core-shell configuration is an efficient interface control method to maximize the interfacial contact between metal Au and semiconductors. However, the wrapping of Au NSs with semiconductors may also block the reaction sites and hinder the absorption of reactants and desorption of products. Therefore, balancing the contact area between Au and semiconductor and the exposure of active sites should take into account to optimize the overall photocatalytic performance [180, 185]. Especially, Wu et al. pointed out that the ability to present appropriate and separate regions, where the photoredox reactions can occur, in contrast with the core@shell structure without such separate regions, was vital for the photocatalytic H_2 production reaction [184]. They fabricated AuNR/TiO_2 nanodumbbells (AuNRs semi-coated with TiO_2) and AuNR@TiO_2 core@shell photocatalysts for H_2 generation under visible light illumination. The AuNR/TiO_2 showed an H_2 evolution rate of 11.6 μmol g^{-1} h^{-1} (**Fig. 13C**), while no H_2 was detected over AuNR@TiO_2 core@shell sample. A plausible mechanism was proposed as follows: upon visible light irradiation, the hot electrons generated in AuNRs flow from AuNRs to TiO_2, and the dumbbell structure enables photoreduction on TiO_2 and then restores charge balance to the Au through oxidation reactions (**Fig. 13D**). In contrast, a fully coated AuNRs in AuNR@TiO_2 core@shell composite disfavors establishing such a complete circuit that allows both electrons and holes to reach their appropriate reaction sites, thereby impeding the continuous flow of the hot charge carriers and suppressing the photocatalytic reaction.

Modulating interfacial interaction between Au NSs and semiconductors has been evidenced to steer the charge transfer dynamics and surface reaction kinetics, thus enhancing the photocatalytic solar-to-fuel conversion efficiency. Despite ongoing progress in this research area, several concerns with interfacial interaction modification require additional attention for future studies. Specifically, most of the research works

pay attention to enhancing the contact area between Au NSs and semiconductors while insights regarding strengthening the interfacial contact are still lacking [179, 181]. Additionally, optimizing the interfacial atomic charge carrier transfer pathways to facilitate the charge transfer via tuning the Schottky barriers or elaborating rational synergy interaction between respective individual components in Au-semiconductor composites could also improve the overall solar energy conversion efficiency, which requires more research in the future. Moreover, metal crystal facets dominated photoactivity and selectivity toward target catalytic reactions have been widely confirmed in semiconductors [186], while the effect of metal Au crystal facets for modulating the catalytic performance of Au-semiconductor photocatalyst remains yet unclear and ambiguous. Moreover, monitoring the charge transfer dynamics process across the interface is of essential importance to designing efficient Au-semiconductor photocatalysts, which requires advanced and powerful techniques, such as transient absorption spectroscopy, time-resolved photoluminescence spectroscopy and transient surface photovoltage.

4.6 Introducing external field

The introduction of external fields, such as thermal, magnetic, microwave, and ultrasonic fields, to catalytic reaction systems have been regarded as one of the powerful strategies to enhance photocatalytic performance [187-189], by which more efficient charge separation and/or hot electrons generated from Au NSs can be realized without changing the properties of the photocatalyst. For Au-based photocatalysts, so far, the thermal, electromagnetic, photo-thermal-magnetic, and piezoelectric external fields have been reported to boost their photocatalytic reactions toward solar-to-fuel conversion [190-196].

For instance, Wang et al. reported that the thermal effect is beneficial for the photocatalytic reduction of CO_2 over Au/TiO_2 photocatalyst [190], in which the heat from solar light and LSPR relaxation of Au nanoparticles could boost the reaction kinetically (**Fig. 14A**). Under NIR radiation, the photothermal effect induced by LSPR relaxation of Au nanoparticles could help to overcome the reaction activation energy to accelerate the photocatalytic CO_2 reduction. However, the poor interfacial contact between Au and TiO_2 cannot separate charge carriers sufficiently, thus leading to limited photoactivity enhancement. To address this issue for further enhancing the overall photocatalytic reaction efficiency, Liu et al. constructed Au@CdS core-shell

composite, where the unique interface characteristics enable thermal-induced hot electrons to inject efficiently from the Au core into the CdS shell [191]. As a result, an H_2 generation rate of 24.0 mmol g^{-1} h^{-1} was achieved over the optimal Au@CdS sample, which is significantly higher than that of CdS with a weak activity (0.1 mmol g^{-1} h^{-1}). This idea was also extended to Au/ZnO [197], SiO_2/CdS [198], MgO/TiO_2 [199] hybrids toward efficient photocatalytic solar-to-fuel conversion.

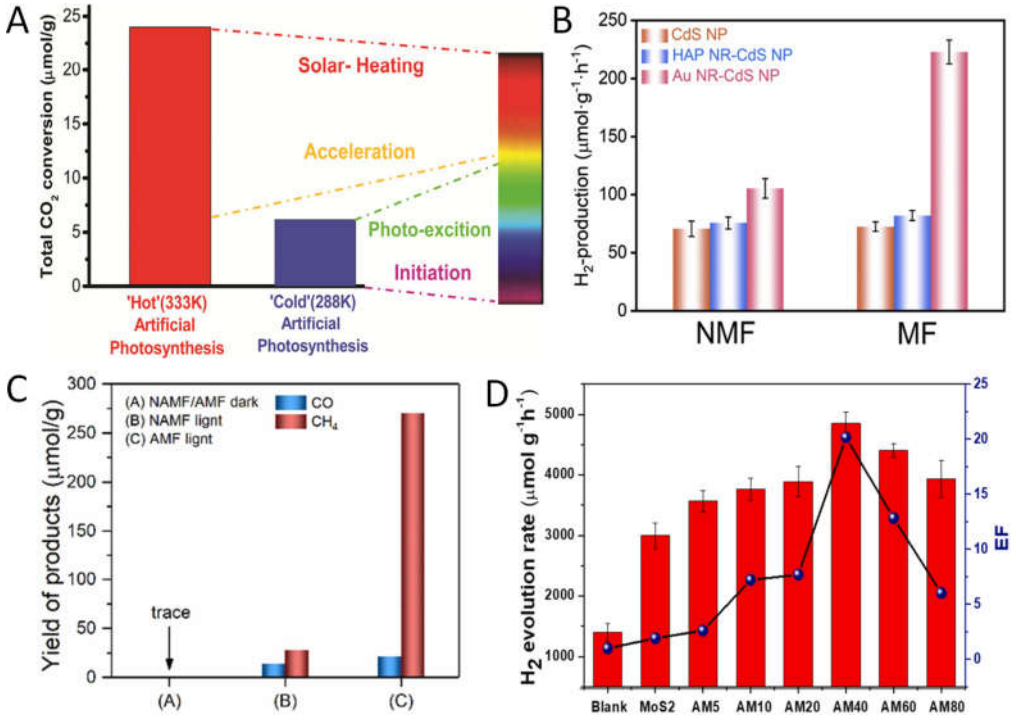

Fig. 14. (A) Schematic illustration of the heat effect on Au-rutile TiO_2 system for photocatalytic CO_2 reduction. Reproduced with permission from ref. [190]. Copyright 2020, Elsevier. (B) Photocatalytic H_2 production over CdS, HAP-CdS and Au NR-CdS with no magnetic field (NMF) or with a magnetic field (MF). Reproduced with permission from ref. [193]. Copyright 2020, Elsevier. (C) The yield of products over NF@ZnO/Au@ZIF-8 under AMF and light illumination with a photo-thermal-magnetic coupling reaction system. Reproduced with permission from ref. [194]. Copyright 2022, Elsevier. (D) H_2 evolution rate over Au@MoS_2 under simultaneous light irradiation and ultrasonic vibration. Reproduced with permission from ref. [200]. Copyright 2021, Elsevier.

Besides the thermal external field, the electromagnetic field has been adopted for improving the photocatalytic performance of Au-based composites [193, 201, 202]. For instance, Gao et al. investigated the effect of an electromagnetic field on photocatalytic

H_2 evolution over Au NRs-CdS core-shell photocatalysts [193]. Without a magnetic field, an H_2 production rate of 105 μmol g^{-1} h^{-1} was obtained over Au NRs-CdS (**Fig. 14B**). Interestingly, the H_2 production rate of Au NRs-CdS improved to 222.8 μmol g^{-1} h^{-1} under a magnetic field (810 Gauss), and no obvious activity changes were observed for both CdS and hydroxyapatite (HAP)-CdS. This was attributed to the electromagnetic induction derived micro-electric potential in Au NRs core to offer an external electric field for facilitating the charge separation in the CdS shell. Inspired by this work, Tu et al. reported that an electromagnetic field nearby Au NSps could enhance the generation and separation of charge carriers to facilitate multiple charge transfer processes, then forming high-grade carbon species (C_2H_6) [201]. Until now, the electromagnetic field has been applied to Au/CuSe [203], Au/$ZnIn_2S_4$/$NaTaO_3$ [204], Au/ZnO/g-C_3N_4 [202] systems for enhancing the photocatalytic solar-to-fuel conversion efficiency.

In addition to a single field, the introduction of multi-fields, such as coupling thermal and magnetic, to achieve continuous high-intensity energy output is demonstrated to further promote the final photocatalytic efficiency of Au-based composite [194, 205]. For example, Tang et al. reported a photo-thermal-magnetic coupling reaction system over Ni foam (NF)@ZnO/Au@imidazole framework-8 (ZIF-8) for photocatalytic CO_2 reduction [194]. Under UV-vis light irradiation, without a magnetic field, the yield of CH_4 over NF@ZnO/Au@ZIF-8 was 28.01 μmol g^{-1} (**Fig. 14C**). While with combined light and alternating magnetic field (AMF), the yield of CH_4 was elevated to 270.12 μmol g^{-1}, showing 10 times enhancement compared to the one without magnetic field. Besides, characterizations showed that, with the multi-fields, the charge transfer efficiency of the NF@ZnO/Au@ZIF-8 catalyst was improved drastically. Therefore, the increased carrier density and charge migration rate, and high-intensity energy output induced by the multi-fields effect contributed to the improved photocatalytic CO_2 reduction activity. Based on these encouraging results, exploiting more multi-fields assisted Au-based photocatalysts is highly expected to further boost the solar-to-fuel conversion performance.

Recently, the piezophototronic effect has been reported to facilitate the photogenerated charge separation, thus boosting the solar to fuel conversion through the building of internal piezoelectric potential [195, 196]. Tu et al. reported that the Au@MoS_2 samples exhibited piezoelectric response at the edge sites of MoS_2 [200], generating a synergistic piezophotocatalytic effect when combined with the LSPR

effect of Au. Specifically, under simultaneous solar light irradiation and ultrasonic vibration, an H_2 evolution rate of 4800 μmol g^{-1} h^{-1} was obtained over Au@MoS_2, as shown in **Fig. 14D**, which was over 11.7-fold higher than the catalyst under solely light irradiation (408 μmol g^{-1} h^{-1}). The underlying mechanism was explained as follows: (1) the Schottky barrier formed at Au and MoS_2 interface greatly reduced the charge recombination rate; (2) the piezopotential induced the injection of hot electrons from Au into MoS_2 to enhance the photocatalytic activity.

To sum up, the introduction of external fields to improve the performance of catalysts has recently attracted extensive attention. Until now, the coupling of heat, ultrasonic, and electric fields into Au-based photocatalytic systems has been explored, while some challenges still need to be addressed in the multi-field systems. For instance, in the presence of heat, the photothermal effect of Au-based catalysts should be fully excluded to identify the exact heat-induced photoactivity enhancement [206]. Furthermore, the introduction of external fields will lead to the complexity of the reaction systems, which may alter the charge transfer pathways and/or reactive pathways and even the reaction mechanism. Therefore, in-situ characterization techniques to provide direct evidence of the intermediate species or charge transfer behaviors are highly desirable. Consequently, exploring suitable external fields and the deep study of external field coupling enhanced mechanisms may open a boulevard to enhance the catalytic performance of Au-semiconductor photocatalysts.

5. Conclusions and perspectives

In summary, Au-modified semiconductor photocatalysts have attracted considerable attention during the past few decades and are widely applied for solar-to-fuel conversion. In this review, we highlight the crucial role of Au NSs in promoting photocatalytic performances and present different strategies proposed for improving the conversion efficiency of Au-based composite catalysts. Despite great progress has been achieved in designing Au-based photocatalysts, it still encounters grand challenges before realizing its full potential toward practical applications. Based on current progress in this research area, some perspectives on the future development for rationally constructing efficient Au-based photocatalysts are proposed.

Firstly, it is accepted that the LSPR properties of An NSs vary with morphology, and the changed LSPR properties can shape the surface electron configuration of semiconductors to mediate the charge generation and transfer, and surface reactions

concerning the adsorption, activation of reactants and selectivity of products [71]. However, the benefits of the Au LSPR effect for promoting the catalytic performance over Au-based photocatalysts for solar-to-energy conversion are not fully exploited. Therefore, the synthesis of irregular shapes of Au NSs with different geometrical natures to improve the LSPR effect can be a promising route to improve the photocatalytic performance of Au-based composites. Recently, the chiroptical effects resulting from the interaction of light with chiral plasmonic NSs have been demonstrated to provide a new platform for asymmetric catalysis [207, 208]. Up to now, different Au NSs with chiroptical effects are reported to modulate the optical activity, and chiral plasmonic resonance of the nanoparticles in the visible to the near-IR region [209, 210]. However, the research on manufacturing the chiral Au NSs to harness their chiroptical effects for solar-to-fuel generation is still lacking. To further improve it, one can construct bimetallic chiral Au nanoparticles with multi-catalytically active centers that exhibit salient features for the conversion of solar energy into chemical fuels [211].

Secondly, phase engineering of nanomaterials (PEN) has stimulated intensive research in recent years, in which the packed ways of metal atoms are engineered to form different phases [41, 42]. The experimental investigations suggest that the crystal phase is one of the key parameters to tuning the physicochemical properties of noble metal nanocrystals, such as optical, mechanical, catalytic, magnetic, electrical, and electronic properties [212]. Various crystal phases of Au NSs, including hexagonal close-packed (hcp, such as 2H, 4H) [43, 44], fct [213], and fcc [214], are synthesized via the PEN and reported to modulate its LSPR in the visible region. For instance, Zhang et al. demonstrated that the unconventional 4H Au exhibited higher photocatalytic dimerization of pNTP than fcc Au, which might be ascribed to the extra contribution from the resonant excitation by the 785 nm laser [140]. However, crystal-phase-dependent photocatalytic performance over Au NSs toward solar fuel generation remains unexplored. Notably, since the phase transformation of 4H-to-fcc can realize via ligand exchange under ambient conditions [44], the effect of light on the structural stability of metastable hcp Au should take into consideration during the photocatalytic solar-to-fuel generation process, which is another appealing research direction to be developed. In one word, the utilization of unconventional Au NSs for converting sunlight into renewable solar fuel via a photocatalytic process is still a virgin land waiting for exploration.

Thirdly, engineering Au with one or multi-metals to form metal alloys with

optimized work functions and exceptional synergetic effects has shown great potential in promoting the photocatalytic performance, product selectivity and stability of Au-based metal (co-)catalysts [146]. Moreover, the introduction of non-noble metal species in Au-based metal alloys could produce efficient (co-)catalysts with reduced cost without losing their photocatalytic performance. Generally, there are five types of mixing patterns for metal alloys, including core-shell alloys, multi-shell alloys, ordered alloys, random homogeneous alloys, and sub-cluster segregated alloys [215, 216]. Since the mixing pattern in Au-based metal alloy may affect the electronic interaction between different metals and the exposure of active sites, it is of crucial importance to disclose the correlation between the mixing pattern of Au alloy and the photocatalytic performance while it is still unclear.

Furthermore, downsizing the Au-based metal alloy into the single-atom level, such as dual atomically dispersed Au (co-)catalysts and single-site heterogeneous (co-)catalysts, could not only improve the atom-utilization efficiency by reducing metal usage but also promote the photocatalytic activity and selectivity due to their unsaturated coordination sites and unique electronic structures [115]. In addition to the bimetallic Au alloy, recently emerged high-entropy metal alloy (HEA), in which five or more principal elements with the concentration of each element being between 35 and 5%, have already exhibited exceptional properties, surpassing the conventional metal alloys [176, 217]. Some Au-based high-entropy alloys are theoretically predicted [218] and experimentally synthesized for electrochemical CO_2 and CO reduction reactions [219, 220], while the CO_2 photoreduction over Au-based HEA remains less studied.

Fourthly, the understanding of charge transfer mechanisms between excited Au NSs and semiconductors should be further clarified during the photocatalytic reaction process. Generally, the photoexcited Au NSs experience three-time constants: (1) the relaxation of electrons through electron-electron scattering (<100 fs), (2) the cooling of hot electrons through electron-phonon scattering (1-10 ps), and (3) the heat dissipation from the Au NSs to the environment through phonon-phonon scattering (~100 ps). Electrons only with high energy before deactivating through electron-electron scattering have a chance to transfer through the surface of Au NSs, leading to poor transfer efficiency. While it is reported that efficient electron transfer can occur in such a short time if electronic coupling with the electron acceptor is large enough. For example, larger TiO_2 particles resulted in longer charge recombination times because of the longer diffusion length of electrons in TiO_2 particles. Therefore, the optimization

of semiconductors supports strengthening the interaction between Au NSs and semiconductors and provides detailed insights into the interfacial charge transfer mechanism are of critical importance.

Fifthly, since the atomic charge carrier transfer efficiency across the interface between the metal Au and semiconductor support ultimately determines the final photocatalytic performance [221], the characterization of the charge separation and transfer process at the Au-support interface is of the top priority and should be monitored via a series of required integral advanced spectroscopic techniques to disclose the underlying reaction mechanism. Specifically, transient absorption spectroscopy (TAS) can reveal the excited state generation and different electron transition processes and then obtain the lifetimes of electrons and holes, which elucidates the charge kinetic information of the photocatalysts. The recombination information of the photogenerated electron-hole pairs can be investigated via time-resolved photoluminescence spectroscopy (TRPL). The above techniques can offer the lifetime of charge carriers while the detailed charge separation dynamics including separation direction, mode and efficiency need to be further characterized by the transient surface photovoltage (TSPV). After the charge separation, the spatial charge distribution at the micro-nano scale in Au-support composite should be confirmed via Kelvin probe force microscopy (KPFM) and/or electrostatic force microscope (EFM), by which the surface charge distribution and quantify the number of photogenerated charges could be directly visualized. Additionally, some technologies, such as *in situ* XPS and light irradiated KPFM, are emerged as advanced tools to *in situ* monitor charge separation and the change of local potential on the surface of photocatalysts induced by the different movement behaviors of photogenerated charges after photoirradiation. The combination of multiple advanced characterization tools could offer comprehensive information regarding the scene of the charge carriers transfer process at the Au-support interface, enabling us to elucidate the fundamental scientific issues and underlying mechanisms during the photocatalytic reaction.

Sixthly, light absorption and scattering of Au NSs can generate non-equilibrium charge carriers, intense electromagnetic near-fields, and heat generation [69]. During the reaction processes, the involvement of hot carriers or/and photothermal effects from the thermalization of these excited carriers via electron-phonon scattering, have been proposed to contribute to the observed reactivity enhancement [72, 87]. Considering that hot carriers reside in a very short lifetime, and the photothermal effect also allows

a much faster cooling so the associated temperature increase is often difficult to predict and measure, it is still changing but important to accurately distinguish photothermal and hot electrons. Baffou et al. proposed some experimental procedures to distinguish photothermal from hot-carrier processes [221], ranging from varying the illumination power and light beam diameter to comparing the effects of various wavelengths. Some more suitable approaches, such as temperature microscopies, kinetic isotope effects, and comparing the product assisted by light and heat, are suggested to adopt for identifying both of them during the photocatalytic solar-to-fuel conversion reactions over Au-based composites.

List of abbreviations

AMF = alternating magnetic field

CB = conduction band

DRIFTS = diffuse reflectance infrared Fourier transform spectroscopy

E_C = valence band energy

E_F = Fermi energy

EFM = electrostatic force microscope

E_V = conduction band energy

fcc = face-centered cubic

hcp = hexagonal close-packed

HEA = high-entropy metal alloy

KPFM = Kelvin probe force microscopy

LSPR = localized surface plasmon resonance

NHE = normal hydrogen electrode

NMF = no magnetic field

NRs = nanorods

NSs = nanostructures

NSps = nanospheres

NIR = near infrared

TAS = transient absorption spectroscopy

T-Au = twin boundary Au

TRPL = time-resolved photoluminescence

TRTEM = high resolution transmission electron microscopy

TSPV = transient surface photovoltage

UV-vis = ultraviolet-visible

VB = valance band

XPS = X-ray photoelectron spectroscopy

e^- = electron

h^+ = hole

h = Planck's constant

ν = light frequency

λ = light wavelength

Φ_B = Schottky barrier energy

Declaration of Competing Interest

The authors declare that they have no known competing financial interests or personal relationships that could have appeared to influence the work reported in this paper.

Acknowledgments

This work was financially supported by the National Natural Science Foundation of China (21902132), the Research Foundation - Flanders (FWO grants 1280021N, 1242922N, 1298323N).

References

[1] J. Liao, Y. Cai, J. Li, Y. Jiang, X. Wang, H. Chen, D. Kuang, J. Energy Chem. 53 (2021) 309-315.

[2] X. Huang, G. Yang, S. Li, H. Wang, Y. Cao, F. Peng, H. Yu, J. Energy Chem. 68 (2022) 721-751.

[3] N. Zhang, C. Han, X. Fu, Y.-J. Xu, Chem 4 (2018) 1832-1861.

[4] C. Wang, C. Zhang, S. Wang, G. Liu, H. Xia, S. Tong, J. He, D. Niu, C. Zhou, K. Ding, Y. Gao, J. Yang, Solar RRL 2 (2018) 1700209.

[5] W. Shang, Y. Li, H. Huang, F. Lai, M.B. Roeffaers, B. Weng, ACS Catal. 11 (2021) 4613-4632.

[6] W. Yuan, Y. Ma, H. Wu, L. Cheng, J. Energy Chem. 65 (2022) 254-279.

[7] A. Fujishima, K. Honda, Nature 238 (1972) 37-38.

[8] H. Zhu, X. Yuan, Q. Yao, J. Xie, Nano Energy 88 (2021) 106306.

[9] B. Weng, Q. Quan, Y.-J. Xu, J. Mater. Chem. A 4 (2016) 18366-18377.

[10] Y. Ding, S. Maitra, C. Wang, S. Halder, R. Zheng, T. Barakat, S. Roy, L. Chen, B. Su, Interdiscip. Mater. 1 (2022) 213-255.

[11] C. Wang, H. Huang, B. Weng, D. Verhaeghe, M. Keshavarz, H. Jin, B. Liu, H. Xie, Y. Ding, Y. Gao, Appl. Catal. B: Environ. 301 (2022) 120760.

[12] J. Wang, H. Zhao, P. Liu, N. Yasri, N. Zhong, M. Kibria, J. Hu, J. Energy Chem.74 (2022) 324-331.

[13] Y. Ding, S. Maitra, C. Wang, R. Zheng, M. Zhang, T. Barakat, S. Roy, J. Liu, Y. Li, T. Hasan, J. Energy Chem. 70 (2022) 236-247.

[14] B. Weng, S. Liu, N. Zhang, Z.-R. Tang, Y.-J. Xu, J. Catal. 309 (2014) 146-155.

[15] C. Wang, Y. Ding, B. Liu, B. Weng, J. Hofkens, M.B.J. Roeffaers, Chem. Comm. 2023, DOI: 10.1039/d3cc00468f.

[16] B. Weng, K.Q. Lu, Z. Tang, H.M. Chen, Y.J. Xu, Nat. Commun. 9 (2018) 1543.

[17] T. Chen, M. Li, L. Shen, M.B. Roeffaers, B. Weng, H. Zhu, Z. Chen, D. Yu, X. Pan, M.-Q. Yang, Front. Chem. 10 (2022) 833784.

[18] C. Wang, B. Weng, Y. Liao, B. Liu, M. Keshavarz, Y. Ding, H. Huang, D. Verhaeghe, J.A. Steele, W. Feng, B-L. Su, J. Hofkens, M.B.J. Roeffaers, Chem. Commun. 58 (2022) 10691-10694.

[19] F. Yu, X. Jing, Y. Wang, M. Sun, C. Duan, Angew. Chem. 133 (2021) 25053-25057.

[20] B. He, C. Bie, X. Fei, B. Cheng, J. Yu, W. Ho, A.A. Al-Ghamdi, S. Wageh, Appl. Catal. B: Environ. 288 (2021) 119994.

[21] Y. Zhang, J. Shi, Z. Huang, X. Guan, S. Zong, C. Cheng, B. Zheng, L. Guo, Chem. Eng. J. 401 (2020) 126135.

[22] M. Wang, Y. Hu, J. Han, R. Guo, H. Xiong, Y. Yin, J. Mater. Chem. A 3 (2015) 20727-20735.

[23] X. Wu, Z. Tang, X. Zhao, X. Luo, S. Pennycook, S. Wang, J. Energy Chem. 61 (2021) 195-202.

[24] H. Wu, X.Y. Kong, X. Wen, S.P. Chai, E.C. Lovell, J. Tang, Y.H. Ng, Angew. Chem. Int. Ed. 60 (2021) 8455-8459.

[25] L. Liu, X. Zhang, L. Yang, L. Ren, D. Wang, J. Ye, Natl. Sci. Rev. 4 (2017) 761-780.

[26] S. Linic, P. Christopher, D.B. Ingram, Nat. Mater. 10 (2011) 911-921.

[27] T.S. Rezende, G.R. Andrade, L.S. Barreto, N.B. Costa Jr, I.F. Gimenez, L. Almeida, Mater. Lett. 64 (2010) 882-884.

[28] A. Henglein, D. Meisel, Langmuir, 14 (1998) 7392-7396.
[29] K. Mallick, Z. Wang, T. Pal, J. Photochem. Photobiol. A: Chem. 140 (2001) 75-80.
[30] K. Okitsu, M. Ashokkumar, F. Grieser, J. Phys. Chem. B 109 (2005) 20673-20675.
[31] X. Wang, Y. Li, H. Wang, Q. Fu, J. Peng, Y. Wang, J. Du, Y. Zhou, L. Zhan, Biosens. Bioelectron. 26 (2010) 404-410.
[32] W. Guo, Y. Pi, H. Song, W. Tang, J. Sun, Colloids Surf. A: Physicochem. Eng. Asp. 415 (2012) 105-111.
[33] N. Elahi, M. Kamali, M.H. Baghersad, Talanta 184 (2018) 537-556.
[34] E.E. Connor, J. Mwamuka, A. Gole, C.J. Murphy, M.D. Wyatt, Small 1 (2005) 325-327.
[35] M. Brust, M. Walker, D. Bethell, D.J. Schiffrin, R. Whyman, J. Chem. Soc., Chem. Commun. (1994) 801-802.
[36] Y. Xiao, B. Shlyahovsky, I. Popov, V. Pavlov, I. Willner, Langmuir, 21 (2005) 5659-5662.
[37] J. Wang, G. Zhu, M. You, E. Song, M.I. Shukoor, K. Zhang, M.B. Altman, Y. Chen, Z. Zhu, C.Z. Huang, ACS Nano 6 (2012) 5070-5077.
[38] B. Wang, J.-H. Wang, Q. Liu, H. Huang, M. Chen, K. Li, C. Li, X.-F. Yu, P.K. Chu, Biomaterials 35 (2014) 1954-1966.
[39] H. Cheng, N. Yang, Q. Lu, Z. Zhang, H. Zhang, Adv. Mater. 30 (2018) 1707189.
[40] N.G. Bastús, J. Comenge, V. Puntes, Langmuir 27 (2011) 11098-11105.
[41] Y. Zhai, P. Han, Q. Yun, Y. Ge, X. Zhang, Y. Chen, H. Zhang, eScience 2 (2022) 467-485.
[42] Y. Chen, Z. Lai, X. Zhang, Z. Fan, Q. He, C. Tan, H. Zhang, Nat. Rev. Chem. 4 (2020) 243-256.
[43] X. Huang, S. Li, Y. Huang, S. Wu, X. Zhou, S. Li, C.L. Gan, F. Boey, C.A. Mirkin, H. Zhang, Nat. Commun. 2 (2011) 1-6.
[44] Z. Fan, M. Bosman, X. Huang, D. Huang, Y. Yu, K.P. Ong, Y.A. Akimov, L. Wu, B. Li, J. Wu, Nat. Commun. 6 (2015) 1-8.
[45] C.-J. Huang, P.-H. Chiu, Y.-H. Wang, K.-L. Chen, J.-J. Linn, C.-F. Yang, J. Electrochem. Soc. 153 (2006) D193.
[46] D.-W. Chou, C.-J. Huang, N.-H. Liu, J. Electrochem. Soc. 163 (2016) D603.
[47] P. Ahrens, M. Zander, U. Hasse, H. Wulff, C. Jeyabharathi, A. Kruth, F. Scholz, ChemElectroChem 5 (2018) 943-957.
[48] Y.-Y. Yu, S.-S. Chang, C.-L. Lee, C.C. Wang, J. Phys. Chem. B, 101 (1997) 6661-

6664.
[49] S. Guo, L. Wang, E. Wang, Chem. Commun. (2007) 3163-3165.
[50] M.V. Sujitha, S. Kannan, Spectrochim. Acta A: Mol. Biomol. 102 (2013) 15-23.
[51] A. Saravanan, P.S. Kumar, S. Karishma, D.-V.N. Vo, S. Jeevanantham, P. Yaashikaa, C.S. George, Chemosphere, 264 (2021) 128580.
[52] P. Nalawade, T. Mukherjee, S. Kapoor, Colloids Surf. A: Physicochem. Eng. Asp. 396 (2012) 336-340.
[53] H. Katas, N.Z. Moden, C.S. Lim, T. Celesistinus, J.Y. Chan, P. Ganasan, S. Suleman Ismail Abdalla, J. Nanotechnol. 2018 (2018).
[54] Y. Sun, Y. Xia, Science 298 (2002) 2176-2179.
[55] S. Chen, Z.L. Wang, J. Ballato, S.H. Foulger, D.L. Carroll, J. Am. Chem. Soc. 125 (2003) 16186-16187.
[56] J. Niu, D. Wang, H. Qin, X. Xiong, P. Tan, Y. Li, R. Liu, X. Lu, J. Wu, T. Zhang, Nat. Commun. 5 (2014) 1-7.
[57] C.S. Ah, Y.J. Yun, H.J. Park, W.-J. Kim, D.H. Ha, W.S. Yun, Chem. Mater. 17 (2005) 5558-5561.
[58] M. Yamamoto, Y. Kashiwagi, T. Sakata, H. Mori, M. Nakamoto, Chem. Mater.17 (2005) 5391-5393.
[59] J. Zhang, J. Du, B. Han, Z. Liu, T. Jiang, Z. Zhang, Angew. Chem. Int. Ed. 45 (2006) 1116-1119.
[60] A. Halder, N. Ravishankar, Adv. Mater. 19 (2007) 1854-1858.
[61] F. Kim, S. Connor, H. Song, T. Kuykendall, P. Yang, Angew. Chem. Int. Ed. 43 (2004) 3673-3677.
[62] J. Zhang, M.R. Langille, M.L. Personick, K. Zhang, S. Li, C.A. Mirkin, J. Am. Chem. Soc. 132 (2010) 14012-14014.
[63] S. Lu, B. Weng, A. Chen, X. Li, H. Huang, X. Sun, W. Feng, Y. Lei, Q. Qian, M.-Q. Yang, ACS Appl. Mater. Interfaces, 13 (2021) 13044-13054.
[64] H. Huang, J. Zhao, B. Weng, F. Lai, M. Zhang, J. Hofkens, M.B. Roeffaers, J.A. Steele, J. Long, Angew. Chem. 134 (2022) e202204563.
[65] Y. Peng, F. Zeng, Y. Cheng, C. Wang, K. Huang, P. Xie, H. Xie, Y. Gao, J. Yang, Org. Electron. 83 (2020) 105736.
[66] B. Weng, J. Zhang, Z.-F. Shi, Z. Tang, L.-S. Zheng, Y.-J. Xu, Langmuir 35 (2019) 5728-5736.
[67] C. Wang, B. Weng, M. Keshavarz, M.-Q. Yang, H. Huang, Y. Ding, F. Lai, I. Aslam,

H. Jin, G. Romolini, B.L. Su, J.A. Steele, J. Hofkens, M.B.J. Roeffaers, ACS Appl. Mater. Interfaces 14 (2022) 17185-17194.
[68] P. Verma, Y. Kuwahara, K. Mori, H. Yamashita, Bull. Chem. Soc. Jpn. 92 (2019) 19-29.
[69] C. Clavero, Nat. Photon. 8 (2014) 95-103.
[70] K.L. Kelly, E. Coronado, L.L. Zhao, G.C. Schatz, J. Phys. Chem. B 107 (2003) 668-677.
[71] C. Yu, X. Xie, N. Zhang, Catal. Sci. Technol. 11 (2021) 425-443.
[72] N.N. Vu, S. Kaliaguine, T.O. Do, ChemSusChem 13 (2020) 3967-3991.
[73] C. Wang, D. Astruc, Chem. Soc. Rev. 43 (2014) 7188-7216.
[74] S. Sarina, E.R. Waclawik, H. Zhu, Green Chem. 15 (2013) 1814-1833.
[75] H. Tada, Dalton Trans. 48 (2019) 6308-6313.
[76] X.-C. Ma, Y. Dai, L. Yu, B.-B. Huang, Light Sci. Appl. 5 (2016) e16017.
[77] R. Long, O.V. Prezhdo, J. Am. Chem. Soc. 136 (2014) 4343-4354.
[78] Z. Lin, X. Wang, J. Liu, Z. Tian, L. Dai, B. He, C. Han, Y. Wu, Z. Zeng, Z. Hu, Nanoscale 7 (2015) 4114-4123.
[79] M. Fang, X. Tan, Z. Liu, B. Hu, X. Wang, Research 2021 (2021).
[80] Z. Liu, W. Hou, P. Pavaskar, M. Aykol, S.B. Cronin, Nano Lett. 11 (2011) 1111-1116.
[81] S. Manzhos, G. Giorgi, J. Lüder, M. Ihara, Adv. Phys.: X 6 (2021) 1908848.
[82] H. Tada, Nanoscale Adv. 1 (2019) 4238-4245.
[83] P. Sudhagar, A. Devadoss, T. Song, P. Lakshmipathiraj, H. Han, V.V. Lysak, C. Terashima, K. Nakata, A. Fujishima, U. Paik, Phys. Chem. Chem. Phys. 16 (2014) 17748-17755.
[84] X. Zhang, Y.L. Chen, R.-S. Liu, D.P. Tsai, Rep. Prog. Phys. 76 (2013) 046401.
[85] M.J. Kale, T. Avanesian, P. Christopher, ACS Catal. 4 (2014) 116-128.
[86] J.R. Adleman, D.A. Boyd, D.G. Goodwin, D. Psaltis, Nano Lett. 9 (2009) 4417-4423.
[87] D. Mateo, J.L. Cerrillo, S. Durini, J. Gascon, Chem. Soc. Rev. 50 (2021) 2173-2210.
[88] J. Cao, T. Sun, K.T. Grattan, Sens. Actuators B: Chem. 195 (2014) 332-351.
[89] C.S. Kumarasinghe, M. Premaratne, Q. Bao, G.P. Agrawal, Sci. Rep. 5 (2015) 1-15.
[90] Y.-C. Pu, G. Wang, K.-D. Chang, Y. Ling, Y.-K. Lin, B.C. Fitzmorris, C.-M. Liu,

X. Lu, Y. Tong, J.Z. Zhang, Nano Lett. 13 (2013) 3817-3823.
[91] Y. Guo, H. Jia, J. Yang, H. Yin, Z. Yang, J. Wang, B. Yang, Phys. Chem. Chem. Phys. 20 (2018) 22296-22307.
[92] Z. Pap, Z.R. Tóth, V. Danciu, L. Baia, G. Kovács, Materials 8 (2014) 162-180.
[93] S. Li, Q.-L. Mo, Y. Xiao, F.-X. Xiao, Coord. Chem. Rev. 477 (2023) 214948.
[94] M. Fujishima, T. Ikeda, R. Akashi, H. Tada, ACS Omega 3 (2018) 6104-6112.
[95] T. Zhang, T. Wang, F. Meng, M.-Q. Yang, S. Kawi, J. Mater. Chem. C 10 (2022) 5400-5424.
[96] S. Han, L. Yu, H. Zhang, Z. Chu, X. Chen, H. Xi, J. Long, ChemCatChem, 11 (2019) 6203-6207.
[97] W. Wang, X. Bai, Q. Ci, L. Du, X. Ren, D.L. Phillips, Adv. Funct. Mater. 31 (2021) 2103978.
[98] J. Zhao, B. Liu, L. Meng, S. He, R. Yuan, Y. Hou, Z. Ding, H. Lin, Z. Zhang, X. Wang, Appl. Catal. B: Environ. 256 (2019) 117823.
[99] E. Ha, L.Y.S. Lee, H.-W. Man, S.C.E. Tsang, K.-Y. Wong, ACS Appl. Mater. Interfaces 7 (2015) 9072-9077.
[100] Y. Wang, J. Zhang, W. Liang, W. Qin, Y. Sun, L. Jiang, Adv. Energy Sustain. Res. 2 (2021) 2100092.
[101] A. Gołąbiewska, A. Malankowska, M. Jarek, W. Lisowski, G. Nowaczyk, S. Jurga, A. Zaleska-Medynska, Appl. Catal. B: Environ. 196 (2016) 27-40.
[102] R. Kaur, B. Pal, J. Mol. Catal. A: Chem. 355 (2012) 39-43.
[103] A. Kumar, K. Kumar, V. Krishnan, Mater. Lett. 245 (2019) 45-48.
[104] M. Rycenga, C.M. Cobley, J. Zeng, W. Li, C.H. Moran, Q. Zhang, D. Qin, Y. Xia, Chem. Rev. 111 (2011) 3669-3712.
[105] K. Yamada, K. Miyajima, F. Mafuné, J. Phys. Chem. C 111 (2007) 11246-11251.
[106] S. Link, M.A. El-Sayed, J. Phys. Chem. B 103 (1999) 4212-4217.
[107] K. Qian, B.C. Sweeny, A.C. Johnston-Peck, W. Niu, J.O. Graham, J.S. DuChene, J. Qiu, Y.-C. Wang, M.H. Engelhard, D. Su, J. Am. Chem. Soc. 136 (2014) 9842-9845.
[108] S. Bera, J.E. Lee, S.B. Rawal, W.I. Lee, Appl. Catal. B: Environ. 199 (2016) 55-63.
[109] Z. Wei, L. Rosa, K. Wang, M. Endo, S. Juodkazis, B. Ohtani, E. Kowalska, Appl. Catal. B: Environ. 206 (2017) 393-405.
[110] M. Teranishi, M. Wada, S.i. Naya, H. Tada, ChemPhysChem 17 (2016) 2813-

2817.
[111] X. Li, C. Liu, D. Wu, J. Li, P. Huo, H. Wang, Chin. J. Catal. 40 (2019) 928-939.
[112] J. Bian, Y. Qu, X. Zhang, N. Sun, D. Tang, L. Jing, J. Mater. Chem. A 6 (2018) 11838-11845.
[113] T. He, A.R.P. Santiago, Y. Kong, M.A. Ahsan, R. Luque, A. Du, H. Pan, Small 18 (2022) 2106091.
[114] A. Taketoshi, M. Haruta, Chem. Lett. 43 (2014) 380-387.
[115] C. Gao, J. Low, R. Long, T. Kong, J. Zhu, Y. Xiong, Chem. Rev. 120 (2020) 12175-12216.
[116] X. Cui, J. Wang, B. Liu, S. Ling, R. Long, Y. Xiong, J. Am. Chem. Soc.140 (2018) 16514-16520.
[117] K. Wang, J. Lu, Y. Lu, C.H. Lau, Y. Zheng, X. Fan, Appl. Catal. B: Environ. 292 (2021) 120147.
[118] Y. Deng, Z. Zhang, P. Du, X. Ning, Y. Wang, D. Zhang, J. Liu, S. Zhang, X. Lu, Angew. Chem. Int. Ed. 59 (2020) 6082-6089.
[119] W. Cheng, H. Su, F. Tang, W. Che, Y. Huang, X. Zheng, T. Yao, J. Liu, F. Hu, Y. Jiang, J. Mater. Chem. A 5 (2017) 19649-19655.
[120] S. Liang, B. Han, X. Liu, W. Chen, M. Peng, G. Guan, H. Deng, Z. Lin, J. Alloys Compd. 754 (2018) 105-113.
[121] P. Shen, S. Zhao, D. Su, Y. Li, A. Orlov, Appl. Catal. B: Environ. 126 (2012) 153-160.
[122] B. Weng, Y. Jiang, H.-G. Liao, M.B. Roeffaers, F. Lai, H. Huang, Z. Tang, Nano Res. 14 (2021) 2805-2809.
[123] L. Zeng, C. Dai, B. Liu, C. Xue, J. Mater. Chem. A 7 (2019) 24217-24221.
[124] Y. Yang, F. Li, J. Chen, J. Fan, Q. Xiang, ChemSusChem 13 (2020) 1979-1985.
[125] T. Wei, Y. Zhu, Y. Wu, X. An, L.-M. Liu, Langmuir 35 (2018) 391-397.
[126] B. Gupta, A.A. Melvin, T. Matthews, S. Dash, A. Tyagi, Renew. Sustain. Energy Rev. 58 (2016) 1366-1375.
[127] T. Tong, B. Zhu, C. Jiang, B. Cheng, J. Yu, Appl. Surf. Sci. 433 (2018) 1175-1183.
[128] Y. Xia, M. Sayed, L. Zhang, B. Cheng, J. Yu, Chem Catal. 1 (2021) 1173-1214.
[129] Q. Mo, L. Zhang, S. Li, H. Song, Y. Fan, C.-Y. Su, J. Am. Chem. Soc. 144 (2022) 22747-22758.
[130] S. Si, H. Shou, Y. Mao, X. Bao, G. Zhai, K. Song, Z. Wang, P. Wang, Y. Liu, Z. Zheng, Angew. Chem. 134 (2022) e202209446.

[131] Y. Cao, L. Guo, M. Dan, D.E. Doronkin, C. Han, Z. Rao, Y. Liu, J. Meng, Z. Huang, K. Zheng, Nat. Commun. 12 (2021) 1-10.

[132] P. Zhou, Y. Chao, F. Lv, J. Lai, K. Wang, S. Guo, Sci. Bull. 65 (2020) 720-725.

[133] H. Ou, G. Li, W. Ren, B. Pan, G. Luo, Z. Hu, D. Wang, Y. Li, J. Am. Chem. Soc. 144 (2022) 22075-22082.

[134] G. Baffou, R. Quidant, F.J. García de Abajo, ACS Nano 4 (2010) 709-716.

[135] Z.-H. Xue, D. Luan, H. Zhang, X.W.D. Lou, Joule 6 (2022) 92-133.

[136] S. Lu, J. Liang, H. Long, H. Li, X. Zhou, Z. He, Y. Chen, H. Sun, Z. Fan, H. Zhang, Acc. Chem. Res. 53 (2020) 2106-2118.

[137] M. Zhou, T. Higaki, G. Hu, M.Y. Sfeir, Y. Chen, D.-e. Jiang, R. Jin, Science 364 (2019) 279-282.

[138] Z. Fan, X. Huang, Y. Han, M. Bosman, Q. Wang, Y. Zhu, Q. Liu, B. Li, Z. Zeng, J. Wu, Nat. Commun. 6 (2015) 1-9.

[139] X. Huang, H. Li, S. Li, S. Wu, F. Boey, J. Ma, H. Zhang, Angew. Chem. Int. Ed. 50 (2011) 12245-12248.

[140] J. Huang, W. Niu, C. Li, C. Tan, P. Yin, H. Cheng, Z. Hu, N. Yang, Q. He, G.-H. Nam, ACS Mater. Lett. 2 (2020) 409-414.

[141] L. Lu, Y. Shen, X. Chen, L. Qian, K. Lu, Science 304 (2004) 422-426.

[142] K. Lu, L. Lu, S. Suresh, Science 324 (2009) 349-352.

[143] E.-J. Gwak, H. Jeon, E. Song, N.-R. Kang, J.-Y. Kim, Acta Mater. 155 (2018) 253-261.

[144] C. Zhang, B.-Q. Chen, Z.-Y. Li, Y. Xia, Y.-G. Chen, J. Phys. Chem. C 119 (2015) 16836-16845.

[145] Q. Xiao, S. Sarina, E.R. Waclawik, J. Jia, J. Chang, J.D. Riches, H. Wu, Z. Zheng, H. Zhu, ACS Catal. 6 (2016) 1744-1753.

[146] Y. Liu, Z. Sun, Y.H. Hu, Chem. Eng. J. 409 (2021) 128250.

[147] H.M. Song, D.H. Anjum, R. Sougrat, M.N. Hedhili, N.M. Khashab, J. Mater. Chem. 22 (2012) 25003-25010.

[148] H. Li, H. Wu, Y. Zhai, X. Xu, Y. Jin, ACS Catal. 3 (2013) 2045-2051.

[149] Y.-C. Tsao, S. Rej, C.-Y. Chiu, M.H. Huang, J. Am. Chem. Soc. 136 (2014) 396-404.

[150] S. Gómez-Graña, B. Goris, T. Altantzis, C. Fernández-López, E. Carbó-Argibay, A.s. Guerrero-Martínez, N. Almora-Barrios, N. López, I. Pastoriza-Santos, J. Pérez-Juste, J. Phys. Chem. Lett. 4 (2013) 2209-2216.

[151] C.-W. Yang, K. Chanda, P.-H. Lin, Y.-N. Wang, C.-W. Liao, M.H. Huang, J. Am. Chem. Soc. 133 (2011) 19993-20000.

[152] C. Zhu, J. Zeng, J. Tao, M.C. Johnson, I. Schmidt-Krey, L. Blubaugh, Y. Zhu, Z. Gu, Y. Xia, J. Am. Chem. Soc. 134 (2012) 15822-15831.

[153] M. Liu, W. Zhou, T. Wang, D. Wang, L. Liu, J. Ye, Chem. Commun. 52 (2016) 4694-4697.

[154] Q. Kang, T. Wang, P. Li, L. Liu, K. Chang, M. Li, J. Ye, Angew. Chem. 127 (2015) 855-859.

[155] A.L. Luna, E. Novoseltceva, E. Louarn, P. Beaunier, E. Kowalska, B. Ohtani, M.A. Valenzuela, H. Remita, C. Colbeau-Justin, Appl. Catal. B: Environ. 191 (2016) 18-28.

[156] Q. Yang, T. Wang, F. Han, Z. Zheng, B. Xing, B. Li, J. Alloys Compd. 897 (2022) 163177.

[157] H. Song, X. Meng, T.D. Dao, W. Zhou, H. Liu, L. Shi, H. Zhang, T. Nagao, T. Kako, J. Ye, ACS Appl. Mater. Interfaces 10 (2018) 408-416.

[158] Z. Zhang, Z. Wang, S.-W. Cao, C. Xue, J. Phys. Chem. C 117 (2013) 25939-25947.

[159] H. Liu, M. Li, T.D. Dao, Y. Liu, W. Zhou, L. Liu, X. Meng, T. Nagao, J. Ye, Nano Energy 26 (2016) 398-404.

[160] A. Malankowska, M.P. Kobylanski, A. Mikolajczyk, O. Cavdar, G. Nowaczyk, M. Jarek, W. Lisowski, M. Michalska, E. Kowalska, B. Ohtani, ACS Sustain. Chem. Eng. 6 (2018) 16665-16682.

[161] J. Ding, X. Li, L. Chen, X. Zhang, S. Sun, J. Bao, C. Gao, X. Tian, J. Mater. Chem. A 4 (2016) 12630-12637.

[162] A. Tanaka, K. Hashimoto, H. Kominami, J. Am. Chem. Soc. 136 (2014) 586-589.

[163] H. An, M. Li, R. Liu, Z. Gao, Z. Yin, Chem. Eng. J. 382 (2020) 122953.

[164] Y. Guo, A. Xu, J. Hou, Q. Liu, H. Li, X. Guo, Nanomaterials, 11 (2021) 3347.

[165] P. Babu, B. Naik, Inorg. Chem. 59 (2020) 10824-10834.

[166] S. Lingampalli, M.M. Ayyub, G. Magesh, C. Rao, Chem. Phys. Lett. 691 (2018) 28-32.

[167] Q. Chen, X. Chen, M. Fang, J. Chen, Y. Li, Z. Xie, Q. Kuang, L. Zheng, J. Mater. Chem. A 7 (2019) 1334-1340.

[168] J. Rodríguez-Torres, C. Gómez-Solís, L.M. Torres-Martínez, I. Juárez-Ramírez, J. Photochem. Photobiol. A.: Chem. 332 (2017) 208-214.

[169] C. Liu, Y. Zhang, J. Wu, H. Dai, C. Ma, Q. Zhang, Z. Zou, J. Mater. Sci. Technol. 114 (2022) 81-89.

[170] Y. Liu, C. Xu, Y. Xie, L. Yang, Y. Ling, L. Chen, J. Alloys Compd. 820 (2020) 153440.

[171] J.N. Stanley, I. García-García, T. Perfrement, E.C. Lovell, T.W. Schmidt, J. Scott, R. Amal, Chem. Eng. Sci. 194 (2019) 94-104.

[172] C. Barrios, E. Albiter, J.G. y Jimenez, H. Tiznado, J. Romo-Herrera, R. Zanella, Int. J. Hydrog. Energy 41 (2016) 23287-23300.

[173] L.-T. Guo, Y.-Y. Cai, J.-M. Ge, Y.-N. Zhang, L.-H. Gong, X.-H. Li, K.-X. Wang, Q.-Z. Ren, J. Su, J.-S. Chen, ACS Catal. 5 (2015) 388-392.

[174] J. Li, P. Yan, K. Li, J. You, H. Wang, W. Cui, W. Cen, Y. Chu, F. Dong, J. Mater. Chem. A 7 (2019) 17014-17021.

[175] Y. Ye, Q. Wang, J. Lu, C. Liu, Y. Yang, Mater. Today 19 (2016) 349-362.

[176] E.P. George, D. Raabe, R.O. Ritchie, Nat. Rev. Mater. 4 (2019) 515-534.

[177] J. Di, B. Lin, B. Tang, S. Guo, J. Zhou, Z. Liu, Small Struct. 2 (2021) 2100046.

[178] S. Bai, W. Jiang, Z. Li, Y. Xiong, ChemNanoMat 1 (2015) 223-239.

[179] S.-F. Hung, Y.-C. Yu, N.-T. Suen, G.-Q. Tzeng, C.-W. Tung, Y.-Y. Hsu, C.-S. Hsu, C.-K. Chang, T.-S. Chan, H.-S. Sheu, Chem. Commun. 52 (2016) 1567-1570.

[180] P. Madhusudan, R. Shi, S. Xiang, M. Jin, B.N. Chandrashekar, J. Wang, W. Wang, O. Peng, A. Amini, C. Cheng, Appl. Catal. B: Environ. 282 (2021) 119600.

[181] A. Wang, S. Wu, J. Dong, R. Wang, J. Wang, J. Zhang, S. Zhong, S. Bai, Chem. Eng. J. 404 (2021) 127145.

[182] S. Patnaik, S. Martha, G. Madras, K. Parida, Phys. Chem. Chem. Phys. 18 (2016) 28502-28514.

[183] S. Bai, X. Li, Q. Kong, R. Long, C. Wang, J. Jiang, Y. Xiong, Adv. Mater. 27 (2015) 3444-3452.

[184] B. Wu, D. Liu, S. Mubeen, T.T. Chuong, M. Moskovits, G.D. Stucky, J. Am. Chem. Soc. 138 (2016) 1114-1117.

[185] H. Tada, T. Mitsui, T. Kiyonaga, T. Akita, K. Tanaka, Nat. Mater. 5 (2006) 782-786.

[186] X. Wu, J. Li, S. Xie, P. Duan, H. Zhang, J. Feng, Q. Zhang, J. Cheng, Y. Wang, Chem 6 (2020) 3038-3053.

[187] C. Hu, S. Tu, N. Tian, T. Ma, Y. Zhang, H. Huang, Angew. Chem. Int. Ed. 60 (2021) 16309-16328.

[188] T. Lv, J. Li, N. Arif, L. Qi, J. Lu, Z. Ye, Y.-J. Zeng, Matter 5 (2022) 2685-2721.

[189] X. Li, W. Wang, F. Dong, Z. Zhang, L. Han, X. Luo, J. Huang, Z. Feng, Z. Chen, G. Jia, ACS Catal. 11 (2021) 4739-4769.

[190] H. Wang, Y. Wang, L. Guo, X. Zhang, C. Ribeiro, T. He, Chin. J. Catal. 41 (2020) 131-139.

[191] J. Liu, J. Feng, J. Gui, T. Chen, M. Xu, H. Wang, H. Dong, H. Chen, X. Li, L. Wang, Nano Energy 48 (2018) 44-52.

[192] B. Zeng, S. Wang, Y. Gao, G. Li, W. Tian, J. Meeprasert, H. Li, H. Xie, F. Fan, R. Li, Adv. Funct. Mater. 31 (2021) 2005688.

[193] W. Gao, Q. Liu, S. Zhang, Y. Yang, X. Zhang, H. Zhao, W. Qin, W. Zhou, X. Wang, H. Liu, Nano Energy 71 (2020) 104624.

[194] Z. Tang, F. Zhu, J. Zhou, W. Chen, K. Wang, M. Liu, N. Wang, N. Li, Appl. Catal. B: Environ. 309 (2022) 121267.

[195] A. Bhardwaj, N.V. Burbure, A. Gamalski, G.S. Rohrer, Chem. Mater. 22 (2010) 3527-3534.

[196] X. Yu, Z. Zhao, J. Zhang, W. Guo, J. Qiu, D. Li, Z. Li, X. Mou, L. Li, A. Li, Small, 12 (2016) 2759-2767.

[197] C. Wang, O. Ranasingha, S. Natesakhawat, P.R. Ohodnicki, M. Andio, J.P. Lewis, C. Matranga, Nanoscale 5 (2013) 6968-6974.

[198] H. Ren, J.-L. Yang, W.-M. Yang, H.-L. Zhong, J.-S. Lin, P.M. Radjenovic, L. Sun, H. Zhang, J. Xu, Z.-Q. Tian, ACS Mater. Lett. 3 (2020) 69-76.

[199] W. Huang, L. Zhang, Z. Li, X. Zhang, X. Dong, Y. Zhang, J. CO_2 Util. 55 (2022) 101801.

[200] C.-Y. Tu, J.M. Wu, Nano Energy 87 (2021) 106131.

[201] W. Tu, Y. Zhou, H. Li, P. Li, Z. Zou, Nanoscale 7 (2015) 14232-14236.

[202] X. Li, H. Jiang, C. Ma, Z. Zhu, X. Song, H. Wang, P. Huo, X. Li, Appl. Catal. B: Environ. 283 (2021) 119638.

[203] L. Ma, D.-J. Yang, X.-P. Song, H.-X. Li, S.-J. Ding, L. Xiong, P.-L. Qin, X.-B. Chen, Solar RRL 4 (2020) 1900376.

[204] J. Zhang, H. Gu, X. Wang, H. Zhang, S. Chang, Q. Li, W.-L. Dai, J. Colloid Interface Sci. 625 (2022) 785-799.

[205] C. Song, Z. Wang, Z. Yin, D. Xiao, D. Ma, Chem Catal. 2 (2021) 52-83.

[206] Q. Lei, S. Yang, D. Ding, J. Tan, J. Liu, R. Chen, J. Mater. Chem. A 9 (2021) 2491-2525.

[207] V.K. Valev, J.J. Baumberg, C. Sibilia, T. Verbiest, Adv. Mater. 25 (2013) 2517-2534.

[208] Y. Wang, J. Xu, Y. Wang, H. Chen, Chem. Soc. Rev. 42 (2013) 2930-2962.

[209] G. Zheng, Z. Bao, J. Pérez-Juste, R. Du, W. Liu, J. Dai, W. Zhang, L.Y.S. Lee, K.Y. Wong, Angew. Chem. Int. Ed. 57 (2018) 16452-16457.

[210] H.-E. Lee, H.-Y. Ahn, J. Mun, Y.Y. Lee, M. Kim, N.H. Cho, K. Chang, W.S. Kim, J. Rho, K.T. Nam, Nature 556 (2018) 360-365.

[211] G. Savitha, R. Saha, G. Sekar, Tetrahedron Lett. 57 (2016) 5168-5178.

[212] Z. Fan, H. Zhang, Acc. Chem. Res. 49 (2016) 2841-2850.

[213] D. Yu, L. Gao, T. Sun, J. Guo, Y. Yuan, J. Zhang, M. Li, X. Li, M. Liu, C. Ma, Nano Lett. 21 (2021) 1003-1010.

[214] Z. Fan, M. Bosman, Z. Huang, Y. Chen, C. Ling, L. Wu, Y.A. Akimov, R. Laskowski, B. Chen, P. Ercius, Nat. Commun. 11 (2020) 1-8.

[215] M. Sankar, N. Dimitratos, P.J. Miedziak, P.P. Wells, C.J. Kiely, G.J. Hutchings, Chem. Soc. Rev. 41 (2012) 8099-8139.

[216] R. Ferrando, J. Jellinek, R.L. Johnston, Chem. Rev. 108 (2008) 845-910.

[217] T.A. Batchelor, J.K. Pedersen, S.H. Winther, I.E. Castelli, K.W. Jacobsen, J. Rossmeisl, Joule 3 (2019) 834-845.

[218] C. Varvenne, W.A. Curtin, Scr. Mater. 142 (2018) 92-95.

[219] S. Nellaiappan, N.K. Katiyar, R. Kumar, A. Parui, K.D. Malviya, K. Pradeep, A.K. Singh, S. Sharma, C.S. Tiwary, K. Biswas, ACS Catal. 10 (2020) 3658-3663.

[220] J.K. Pedersen, T.A. Batchelor, A. Bagger, J. Rossmeisl, ACS Catal. 10 (2020) 2169-2176.

[221] F. Chen, T. Ma, T. Zhang, Y. Zhang, H. Huang, Adv. Mater. 33 (2021) 2005256.

Graphical Abstract

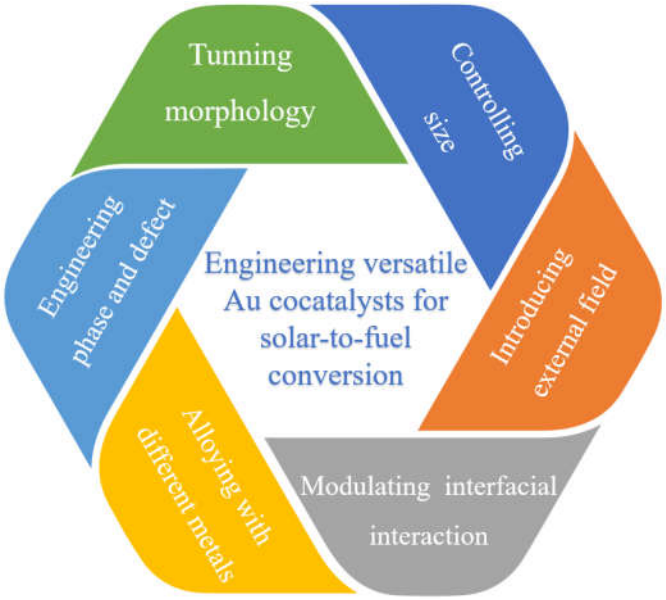

We summarize the recent reports in engineering Au-based composites for photocatalytic solar-to-fuel conversion, focusing on discussing the modification strategies of Au nanostructures (NSs) that are used to enhance the overall photocatalytic performance, including controlling the Au NS morphology, size, crystal phase, defect engineering, alloying with different metals, modulating interfacial interaction, and introducing an external field.